Chapter 8
Characterization of Calcium Phosphates Using Vibrational Spectroscopies

Christian Rey, Olivier Marsan, Christèle Combes, Christophe Drouet, David Grossin, and Stéphanie Sarda

Abstract Vibrational spectroscopies are extensively used for the characterization of calcium phosphates either as natural biological minerals (bone, teeth, ectopic calcifications) or as biomaterials (bioceramics, coatings, composites). The present review begins with a theoretical description of expected spectra for the main calcium phosphate phases (i.e., brushite, monetite, octacalcium phosphate, tricalcium phosphates, apatites, amorphous calcium phosphate) followed by the analysis of real spectra, line positions and assignments, and observed anomalies. In the second part, the spectra of complex well-crystallized ion-substituted apatites and other calcium phosphates, as well as solid solutions, are investigated, and the information gained regarding the substitution types and ion distributions are derived. Finally, we will examine and interpret the spectra of nanocrystalline apatites considering the ion substitution effects and the existence of a surface hydrated layer. Quantification processes and spectra treatments are briefly presented and discussed. Examples of the use of vibrational spectroscopies for biomaterials and biominerals characterization will be detailed for coating evaluations, including spectroscopic imaging, following up on mineral cement setting reactions, adsorption studies, near infrared investigations of surface water, residual strains determinations in bone, orientation of apatite crystals in biological tissues, and crystallinity and maturity of bone mineral.

Keywords FTIR and Raman spectra • Phosphate • Carbonate • Apatite • Coating • Cements • Adsorption • Mechanical strains • Crystal orientation • Bone crystallinity and maturity

C. Rey (✉) • O. Marsan • C. Combes • C. Drouet • D. Grossin • S. Sarda
CIRIMAT-Carnot Institute, University of Toulouse, UMR CNRS-UPS-INPT 5085, ENSIACET, Toulouse, France
e-mail: christian.rey@ensiacet.fr

B. Ben-Nissan (ed.), *Advances in Calcium Phosphate Biomaterials*, Springer Series in Biomaterials Science and Engineering 2, DOI 10.1007/978-3-642-53980-0_8,

8.1 Introduction

Calcium phosphate (Ca–P) biominerals, especially apatites, are complex structures affording many ion substitutions and vacancies, which may be poorly crystallized. Their study by diffraction techniques does not always give information on fine structural details such as the presence and location of CO_3^{2-}, HPO_4^{2-}, or OH^- groups. Vibrational spectroscopies bring, in addition to structural identification, this valuable information and may be used for a quantitative determination on a very limited amount of material. They may also yield, in favorable cases, information on the orientation of molecular species and crystals; in addition, microscopic techniques can also be used for local investigations on biological tissues or materials, and they allow a rather accurate mapping of specific mineral characteristics.

Several techniques involve transitions between vibrational levels. This review is mainly focused on FTIR and Raman spectroscopies, which are used extensively. Vibrational spectra of different Ca–P of biological interest will first be described with an emphasis on apatites. The effect of ion substitutions and vacancies will be illustrated, showing how local environments disturb the vibrational spectra. This phenomenon can be used for the characterization of surface species in nanocrystalline compounds. Many other uses of vibrational spectroscopies have been published, for example, in adsorption studies, follow-up of calcium phosphate cement setting, analyses of coatings, near infrared (NIR) investigations of surface water, or biological mineralizations. These will be briefly discussed in the last section of this chapter.

8.2 Basic Spectra and Line Assignments

8.2.1 Theoretical Considerations

A vibration is defined by a periodic variation of the interatomic distance in a compound. In the simple case of a diatomic molecule, A-B, the vibration frequency can be modeled using the simple Hook's law in the approximation of a harmonic oscillator. The frequency of vibration, ν, is given by

$$\nu = \frac{1}{2\pi c}\sqrt{\frac{k}{\mu}}$$

where κ is the force constant associated with the chemical bond and μ is the reduced mass: $\mu = m_A{}^*m_B/(m_A + m_B)$ with m_A and m_B the mass of atoms A and B. For more complex molecular species, different types of vibrations are possible, which can be determined theoretically [1]. Two types of vibrations with different energy domains are recognized for molecular species other than diatomic

Table 8.1 Vibrational characteristics of molecular ions involved in calcium phosphates

Molecular ion (symmetry)	Vibrational domains, symmetry, and activity of the free ions (R: Raman activity and IR: infrared activity)					
	ν_1	ν_2	ν_3		ν_4	
PO_4^{3-} (T_d)	A_1 (R)	E (R)	T_2 (IR, R)		T_2 (IR, R)	
Position (cm^{-1})	938	420	1,017		567	
HPO_4^{2-} (C_{3v})	A	E	A	+ E	A	+ E
	(IR, R)	(IR, R)	(IR, R)	(IR, R)	(IR, R)	(IR, R)
Positions (cm^{-1})	988	394	862	1,076	537	537
CO_3^{2-} (D_{3h})	A'_1	A''_2	E′		E′	
	(R)	(IR)	(IR, R)		(IR, R)	
Positions (cm^{-1})	1,064	879	1,415		680	

ones: stretching vibrations, corresponding to an elongation of chemical bonds, and bending vibrations, corresponding to angular variation between two chemical bonds. Stretching vibrations exhibit a higher energy than the bending ones.

In crystalline solids several types of vibration may occur. In addition to acoustic modes, two main types are identified, "internal vibrations" associated with molecules and molecular ions with covalent bonds that are present in the solid and "external vibrations" corresponding to the vibrations of species and ions in their crystallographic site [2–4]. Internal vibrations are generally close to the vibration energy of the free molecule/ions and allow the identification of molecular species in the solid. However, variations will appear in the energies of internal vibrations and in their relative intensities which depend on the environments of these molecular species in the solid. Such variations allow a precise identification of mineral structures in most cases. Although external vibration modes also depend on the crystal structure, their energy is lower than that of internal vibrations, and they are more easily accessed using Raman spectroscopy. Among these external vibrations, two types of movements may be recognized: translation modes and libration modes, which can be viewed as partial rotation of molecular groups in the crystal. Libration movements of OH^- ions and H_2O molecules occur at a relatively high energy compared to non-protonated molecules, and the corresponding lines are frequently found among the internal vibrations of other species like phosphate or carbonate. To complete the description of vibrational spectra, overtone and combination lines, which involve multi-quanta excitations, can be observed, although with much weaker intensities than fundamental lines.

The main molecules and molecular ions found in calcium phosphates are orthophosphate groups: PO_4^{3-}, HPO_4^{2-}, $H_2PO_4^-$ and also H_2O, OH^-, CO_3^{2-}. The vibrational characteristics of the "free" CO_3^{2-} and PO_4^{3-} ions are shown in Table 8.1 [5, 6], with the symmetry group and vibrational domains. We will use the denominations of the spectroscopic domains of the free molecules/ions to describe and discuss the different spectra in this paper. Although specific domains can be used for protonated phosphate species [5, 7], the P–O vibrational regions remain close to those of the PO_4^{3-} group and they will be discussed by reference

to this ion. In protonated species additional lines are expected due to the O–H bond. The stretching of the O–H bonds in HPO_4^{2-} and $H_2PO_4^-$ groups are generally broad and appear with a low to medium intensity. However, the P-(OH) bonds in HPO_4^{2-} and $H_2PO_4^-$ are longer and weaker than the P–O bond in the PO_4^{3-} ion, and the corresponding stretching bands are shifted towards lower wavenumbers. These bands are very sensitive to hydrogen bonding [5, 8, 9]. In contrast the weakening of the P–OH bond is associated with a strengthening of the remaining P–O bonds, whose stretching vibrations are shifted towards higher wavenumbers, whereas bending vibrations are shifted towards lower wavenumbers. The symmetry alterations induced by protonation occurring in HPO_4^{2-} can conveniently be described using distorted PO_4 edifices belonging to C_{3v} symmetry (although the symmetry of the real free ions is lower). These species have been included in Table 8.1.

The vibrational modes of "free" molecular ions and molecules are conveniently determined using molecular group theory [1], which is used to name and distinguish the vibrational modes. Group theory also allows determination of the infrared (IR) and Raman (R) observance of the vibrational modes, their "activity," which is related to the physical interactions between electromagnetic radiations and vibrational energy levels involved in these spectroscopic methods [2–4].

In crystalline solids two main alterations have been identified: the site symmetry effect and the factor group symmetry [2–4]. The site symmetry effect corresponds to an alteration in vibrational energy levels due to the symmetry lowering of the "free" molecule or polyatomic ion related to its position in a well-defined crystallographic site; these effects are shown in Tables 8.2, 8.3, and 8.4 for different crystalline calcium phosphates in different structures [5, 9–14]. Considering PO_4^{3-} ions in apatites with a hexagonal unit cell (space group $P6_3/m$; Table 8.3), for example, the site symmetry is C_s, as only a symmetry plane is preserved from the original tetrahedral symmetry. In consequence, the degeneracy of vibrational modes E (degeneracy: 2) and T_2 (degeneracy: 3) of the "free" PO_4^{3-} species is raised, and instead of one vibrational level, several non-degenerated modes occur. All these vibrational modes are active in IR and R and a "splitting" of the ν_2, ν_3, and ν_4 lines is predicted. In addition, ν_1 and ν_2 modes are now active in IR, although they were not observed for the free ion.

The factor group treatment provides a complete prediction of the vibrational levels of a crystal for both internal and external vibration modes. This approach takes into consideration the whole content of the unit cell, including the correlations between the vibrations of similar groups in a crystal that may interfere with each other in a confined environment. These considerations result in additional vibrational levels of molecules and molecular ions as shown in Tables 8.2, 8.3, and 8.4. The number of predicted lines may vary considerably according to the structure. For compounds containing HPO_4^{2-}, OH^- ions, and water molecules, line broadenings are observed related to hydrogen bonding. In addition, libration transitions, which have not been considered here, appear in addition to bending and stretching lines.

The factor group may lead to weak shifts so, when numerous lines are expected, individual components are hindered by line broadening and cannot be distinguished.

Table 8.2 Internal vibrations of phosphate groups in non-apatitic calcium phosphates of interest (PO_4^{3-}-containing compounds)

Tetracalcium phosphate (TTCP); $Ca_4(PO_4)_2O$; monoclinic $P2_1$ [10]			
	ν_1 PO_4	ν_2 PO_4	ν_3, ν_4 PO_4
Site symmetry: C_1	A(IR-R)	2A(IR-R)	3A(IR-R)
Factor group: C_2	2A(IR-R)	4A(IR-R)	6A(IR-R)
	2B(IR-R)	4B(IR-R)	6B(IR-R)
Number of lines IR	4	8	12
Number of lines R	4	8	12
α-Tricalcium phosphate (α-TCP); $Ca_3(PO_4)_2$; monoclinic $P2_1/a$ [12]			
	ν_1 PO_4	ν_2 PO_4	ν_3, ν_4 PO_4
Site symmetry: C_1	A(IR,R)	2A(IR-R)	3A(IR-R)
Factor group: C_{2h}	$12A_g$(R)	$24A_g$ (R)	$36A_g$(R)
	$12A_u$(IR)	$24A_u$ (IR)	$36A_u$(IR)
	$12B_g$(R)	$24B_g$ (R)	$36B_g$(R)
	$12B_u$(IR)	$24B_u$ (IR)	$36B_u$(IR)
Number of lines IR	24	48	72
Number of lines R	24	48	72
β-Tricalcium phosphate (β-TCP); $Ca_3(PO_4)_2$; trigonal R3c [12]			
	ν_1 PO_4	ν_2 PO_4	ν_3, ν_4 PO_4
Site symmetry C_3	A(IR-R)	E(IR-R)	A(IR-R)
			E(IR-R)
Site symmetry C_1	A(IR-R)	2A(IR-R)	3A(IR-R)
Factor group C_{3v}	$3A_1$(IR-R)	$2A_1$(IR-R)	$5A_1$(IR-R)
	E(IR-R)	4E(IR-R)	5E(IR-R)
Number of lines IR	4	6	10
Number of lines R	4	6	10

Molecular group theory, site symmetry, and factor group treatments do not allow the prediction of spectra with their line positions and intensities.

This information can be provided by quantum chemistry calculations [15]. For mineral structures with disordered or partially occupied sites and for solid solutions, factor group theory is more difficult to apply. For amorphous structures like amorphous calcium phosphates, the spectra prediction may rely on the symmetry of basic structural units, Posner's clusters (Table 8.5) [16], although the S_6 symmetry of these clusters has been discussed and lower symmetry, C_1 or C_3, has been proposed depending on the environment [17].

8.2.2 Spectra of Well-Defined Stoichiometric Calcium Phosphates

The FTIR and Raman spectra of the most important calcium phosphates are shown in Figs. 8.1 and 8.2. Line positions are reported in Tables 8.6 and 8.7.

Table 8.3 Internal vibrations of phosphate groups in apatites for different structures and symmetries

Apatite; hexagonal $P6_3/m$ [11]			
	ν_1 PO_4	ν_2 PO_4	ν_3, ν_4 PO_4
Site symmetry: C_s	A′(IR-R)	A′(IR-R), A″(IR-R)	2A′(IR-R), A″(IR-R)
Factor group: C_{6h}	A_g (R), E_{2g} (R), B_u E_{1u}(IR),	A_g(R), E_{2g}(R), B_u, E_{1u}(IR), B_g, E_{1g}(R), A_u (IR), E_{2u}	$2A_g$(R), $2E_{2g}$(R), $2B_u$, $2E_{1u}$(IR), B_g, E_{1g}(R), A_u (IR), E_{2u}
Number of lines IR	1	2	3
Number of lines R	2	3	5
Apatite; hexagonal $P6_3$ [12]			
	ν_1 PO_4	ν_2 PO_4	ν_3, ν_4 PO_4
Site symmetry: C_1	A (IR,R)	2A (IR-R)	3A (IR-R)
Factor group: C_6	A(IR-R), B, E_1(IR-R), E_2(R)	2A(IR-R), 2B, $2E_1$(IR-R), $2E_2$(R)	3A(IR-R), 3B, $3E_1$(IR-R), $3E_2$(R)
Number of lines IR	2	4	6
Number of lines R	3	6	9
Apatite; monoclinic $P2_1/b$			
	ν_1 PO_4	ν_2 PO_4	ν_3, ν_4 PO_4
Site symmetry C_1	A(IR,R)	2A(IR-R)	3A(IR-R)
Factor group C_{2h}	$3A_g$(R), $3B_g$(R), $3A_u$(IR), $3B_u$(IR)	$6A_g$(R), $6B_g$(R), $6A_u$(IR), $6B_u$(IR)	$9A_g$(R), $9B_g$(R), $9A_u$(IR), $9B_u$(IR)
Number of lines IR	6	12	18
Number of lines R	6	12	18

Very often for complex structures, the assignments are difficult to obtain due to the superimposition of elementary fundamental vibrations. Theoretical calculated spectra can, in principle, be obtained if the crystal structure is known, and a few reports have been published on this subject [15].

Generally speaking, the spectra observed for well-crystallized stoichiometric calcium phosphates like apatite correspond to the theoretical prediction, although some anomalies can be noted like the observation of superimposed E_{2g} and A_g modes for the apatite spectra in the ν_1 PO_4^{3-} domain in Raman or other anomalies [11]. Detailed investigations have discussed the occurrence of faint lines revealed by second derivatives of the spectra and the adequacy of the $P6_3/m$ model for hexagonal hydroxyapatite [11, 20, 21] (factor group C_{6h}), compared to the real local symmetry (factor group C_6). The structure of stoichiometric hydroxyapatite, corresponding to a monoclinic unit cell, space group $P2_1/b$, should theoretically lead to spectra with additional lines which are not all observed. The ordering of OH^- anions in the structure, related to the monoclinic superstructure, seems to have little effect on the vibration movements of the PO_4^{3-} ions, which is very analogous in hydroxyapatite to that of a truly $P6_3/m$ symmetry like that of fluorapatite [11, 22].

The spectra of tricalcium phosphates (TCP) and tetracalcium phosphates (TTCP) are particularly complex, and all predicted lines cannot be distinguished and identified due to superimposition, except for the ν_1 lines of TTCP which are

Table 8.4 Internal vibrations of phosphate groups in calcium phosphates of interest (HPO_4^{2-}-containing compounds)

Octacalcium phosphate (OCP); $Ca_8(PO_4)_4(HPO_4)_2, 5H_2O$; triclinic P−1 * HPO_4^{2-} [14]			
	ν_1 PO_4	ν_2 PO_4	ν_3, ν_4 PO_4
Site symmetry: C_1	A(IR,R)	2A(IR, R)	3A(IR, R)
Factor group: C_i	4+2*A_g(IR)	8+4*A_g(IR)	12+6*A_g(IR)
	4+2*B_u (R)	8+4*B_u(R)	12+6*B_u(R)
Number of lines IR	4+2*	8+4*	12+6*
Number of lines R	4+2*	8+4*	12+6*
Anhydrous dicalcium phosphate (DCPA) or monetite; $CaHPO_4$; triclinic P−1			
Site symmetry: C_1	A(IR, R)	2A(IR, R)	3A(IR, R)
Group factor: C_i	2A_g(R)	4A_g(R)	6A_g(R)
	2A_u(IR)	4A_u(IR)	6A_u(IR)
Number of lines IR	2	4	6
Number of lines R	2	4	6
Dicalcium phosphate dihydrate (DCPD) or brushite; $CaHPO_4$; monoclinic Ia [5]			
Site symmetry: C_1	A(IR-R)	2A(IR-R)	3A(IR-R)
Site symmetry: C_s	A′(IR-R)	A′(IR-R)	2A′(IR-R)
		A″(IR-R)	A″(IR-R)
Factor group: C_s	A′(IR-R)	2A′(IR-R)	3A′(IR-R)
	A″(IR-R)	2A″(IR-R)	3A″(IR-R)
Number of lines IR	2	4	6
Number of lines R	2	4	6

Table 8.5 Vibrations of phosphate groups in amorphous calcium phosphate (ACP) assuming a S_6 symmetry of the Posner's clusters [16]

	ν_1 PO_4	ν_2 PO_4	ν_3, ν_4 PO_4
Symmetry S_6	A_u(IR), E_u(IR)	2A_u(IR), 2E_u(IR)	3A_u(IR), 3E_u(IR)
	A_g(R), E_g(R)	2A_g(R), 2E_g(R)	3A_g(R), 3E_g(R)
Number of lines IR	2	4	6
Number of lines R	2	4	6

relatively thin and well resolved. The case of α-TCP is special due to a very large unit cell with numerous phosphate groups, giving numerous lines with a poor resolution. Strong lines are observed in the FTIR ν_2 PO_4 domain of TTCP, like in oxyapatite [23], possibly related to the presence of oxide ions in these structures.

Other types of lines can be observed corresponding to the libration movements of protonated species like OH^- ions for hydroxyapatite or H_2O- and HPO_4^{2-}-related lines for brushite and octacalcium phosphates. On Raman spectra several external vibrations can be detected at low wavenumbers. Several differences between the spectra of different calcium phosphate phases allow their identification and, to some extent, their quantification. Overtone and combination bands can be seen

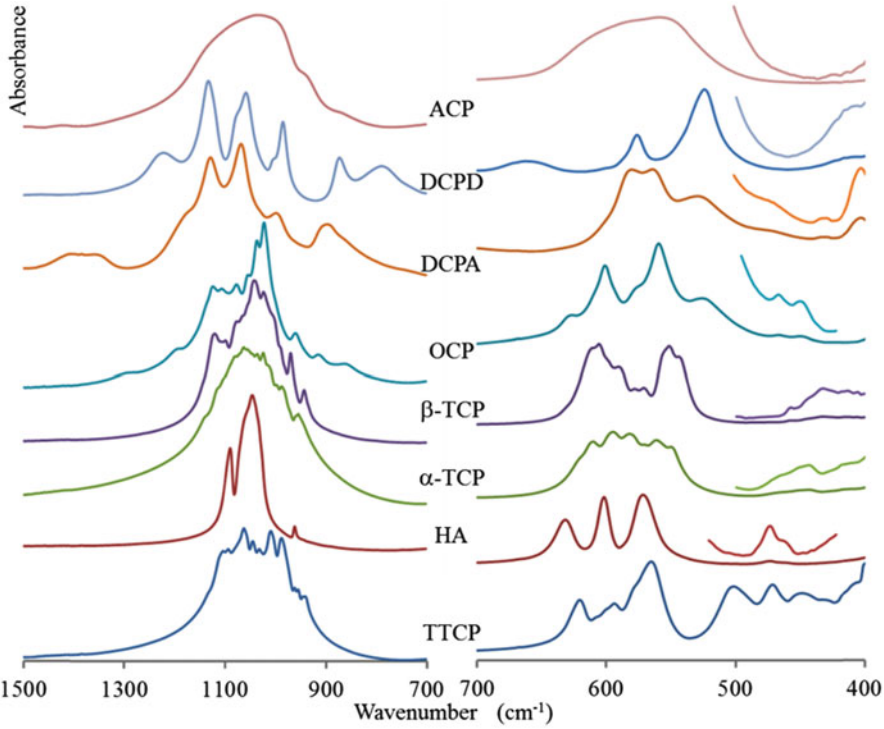

Fig. 8.1 FTIR spectra of calcium phosphates in the domains of internal vibrations of phosphate ions

on some spectra. For hydroxyapatite and related compounds, the most frequently observed overtone/combination is a group of lines at 2,200–1,950 cm^{-1} [11].

These weak intensity lines do not seem to have received much attention and they are sometimes misinterpreted. Overtone and combination bands of protonated molecules are also used in near infrared (NIR) characterization of calcium phosphates. Lines assignments have been proposed in the case of the simplest spectra like apatite [11, 12, 20, 22, 24, 25]. For the amorphous calcium phosphate, the lines appear very broad and dissymmetric, suggesting the existence of several components. It seems however difficult, using FTIR and Raman data, to contribute to the discussion concerning the symmetry of real Posner's clusters.

8.3 Methods and Techniques

The vibrational spectra of solids are relatively complex, and several techniques have been used to improve band resolution and assignment. Spectra obtained at low temperatures, for example, may show narrower lines, improving the band

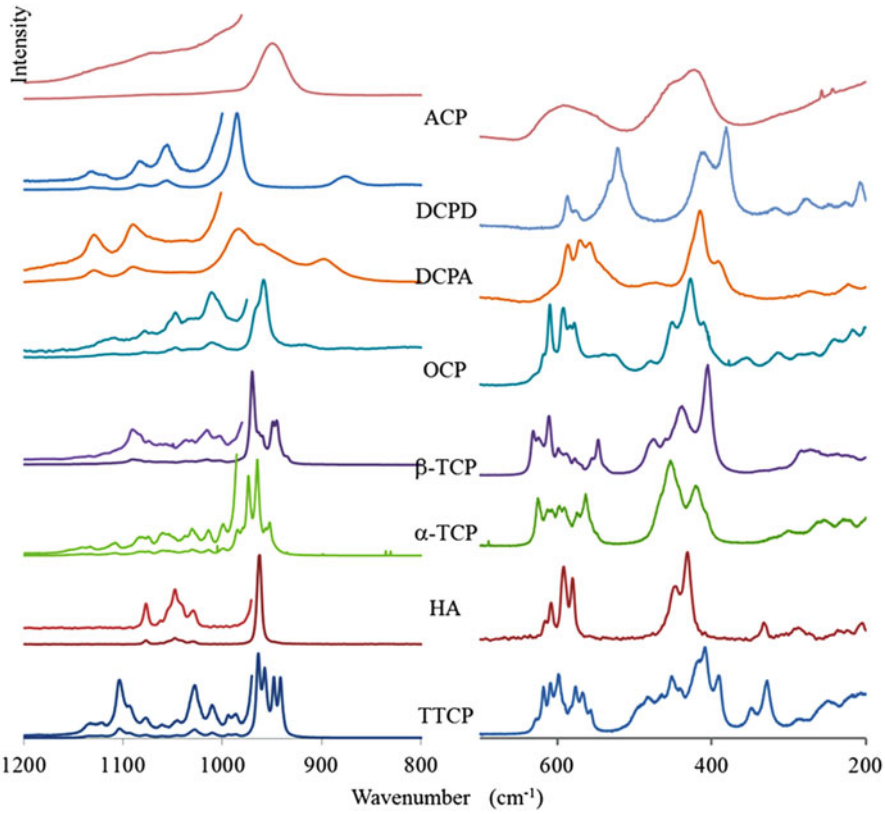

Fig. 8.2 Raman spectra of calcium phosphates in the domains of internal vibrations of phosphate ions (for comparison purposes the wavenumber axis is in reverse order, like for the FTIR spectra)

resolution in certain cases [9, 18]. Among specific techniques applied to vibrational spectroscopies are isotopic substitutions and the use of dichroic properties. Data computing is also largely used, as in other domains of spectroscopy.

8.3.1 Isotopic Substitutions

One of the strengths of vibrational spectroscopies is the possible use of stable isotopic substituted molecules or molecular ions that can be incorporated into a material as molecular probes [18, 24]. Isotopic substitutions allow the identification of vibrating groups when some doubt or suspicion is raised, follow-up of chemical reactions or transformations of calcium phosphates, or simply shifts of weak hidden lines superimposed on other absorption bands.

Table 8.6 FTIR line positions of calcium phosphates (cm^{-1}; *m* medium, *s* strong, *sh* shoulder, *v* very, *w* weak)

	TTCP	HA	α-TCP	β-TCP	OCP	DCPA	DCPD	ACP
ν_3 PO_4						1,400 w		
						1,350 w		
					1,295 w		1,215 m	
					1,193 w	1,175 m,sh		
					1,137 vvw	1,128 s	1,132 s	
				1,119 s	1,121 s			
	1,105 w				1,103 s			
	1,093 w	1,092 s		1,094 w,sh				
	1,073 w			1,080 w,sh	1,077 s		1,070 s	
	1,062 s		1,055 s		1,055 s	1,064 s	1,060 s	
	1,046 s	1,040 vs	1,039 s	1,041 vs				1,040 s
	1,033 m		1,025 s		1,037 s			
			1,013 s		1,023 s			
	1,010 s		997 s	1,010 w,sh	1,000 vvw		1,000 w,sh	
	989 s		984 s					
ν_1 PO_4				972 s		992 m	984 s	
	962 w	962 w			962 w			
	956 w		954 m					
	946 w			945 m				949 w,sh
	941 w							
P-OH of HPO_4^{2-}					917 w			
					861 w	892 m	872 m	
ν_4 PO_4	620 w		613 m		627 vw			
	594 w	601 m	597 m	602 m	601 m			
			585 m	589 w				
	571 s	575 m,sh	563 m		575 w	576 s	577 m	
		561 m	551 m	550 m	560 m	563 s		560 m
	501 w			541 m	524 w	525 m	526 s	
ν_2 PO_4	471 m	472 vw	471 w			480		
		462 sh	463 w		466 vw			
			454 w					
	450 w		430 w	432 vw	449 vw	428 vw	418 sh	
	429 w		415 w			405 m	400 m	
	399 m					398 sh		
References	[10]	[12]	[13]	[12]	[14]	[12]	[18]	

The isotopic shift (position ratio between identical vibration modes of the unsubstituted and isotopic substituted molecules) can vary according to the atom substituted in the molecule and the vibrational mode considered. For diatomic vibrators like the OH^- ion, the shift between OH^- and its deuterated equivalent OD^- is given using Hook's derived formula. The position ratio between the protonated and deuterated ion stretching line is theoretically close to 0.7276, the square root of the reduced mass ratios, which in fact is observed experimentally.

Table 8.7 Raman line positions of calcium phosphates (cm^{-1}; *m* medium, *s* strong, *sh* shoulder, *v* very, *w* weak)

	TTCP	HA	α-TCP	β-TCP	OCP	DCPA	DCPD	ACP
ν_3 PO_4						1,131 m	1,132 vw	
	1,119 vw						1,119 vw	1,118 w
	1,101 w				1,112 w			
	1,091 sh	1,077 w	1,077 w	1,090 w	1,079 vw	1,094 m	1,079 w	
	1,076 vw	1,064 w					1,061 m	
		1,057 w	1,058 w		1,052 w			
	1,045 vw	1,048 w			1,048 w			1,050 w
		1,041 w						
		1,034 w			1,036 vw			
	1,026 w	1,029 w	1,027 w		1,027 vw			
	1,008 w		1,012 w	1,015 w	1,011 m			
			998 w		1,005 w,sh			
ν_1 PO_4	983 vw		976 s					
	961 vs	964 vs	964 s	970 s	966 s	988 s	986 s	
	956 vs		954 sh	948 s	959 vs			
	946 s							951 s
	940 s							
P-OH st. of HPO_4^{2-}					916 w	900 m		
					874 w		878 m	
ν_4 PO_4	615 vw	614 w	620 w		619 vw			
	608 vw	607 w	610 w	612 w	609 mw			
	597 w	591 w	593 w		591 m	588 m	588 w	594 m
	576 vw	580 w	577 w		577 m	563 m		
	566 sh		563 w					
	556 vw			549 w				
	495 sh				523 w, b		525 w	
ν_2 PO_4	481 sh			480 w				
	463 sh	448 w	451 w		451 m			451 m
	449 w	433 w		439 w				
	414 sh		421 w		427 m	420 w		419 m
	407 w			408 w	409 m		411 w	
	389 w				353 w	394 w	381 w	
References	[10]	[19]	[13]	[19]	[14]	[20]	[19]	

For more complex molecules, the isotopic shift depends only on the mass ratios of the atoms and can be determined according to the Teller–Redlich product rule [26]. The replacement of ^{12}C by ^{13}C in the carbonate ion, for example, gives different shifts depending on the vibration domain. The line position ratios are, respectively, 1,000, 0.9686, 0.9723, and 0.9963 for the ν_1, ν_2, ν_3, and ν_4 domains. The replacement of ^{16}O by ^{18}O in PO_4 groups has been used in early studies [24]. However, as a total substitution of ^{16}O by ^{18}O could not be achieved, the spectra were rendered more complex by virtue of the different possible substitutions.

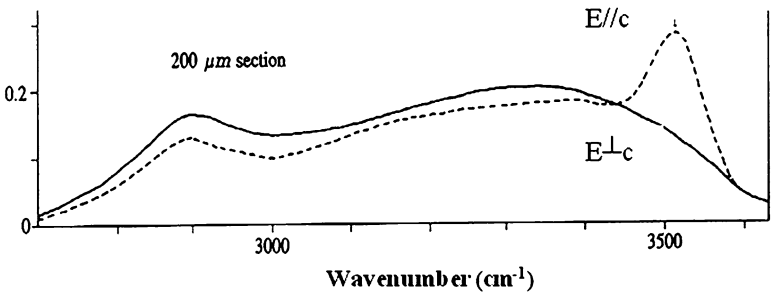

Fig. 8.3 Example of dichroism on dahlite monocrystals (IR spectra). *Dotted line*: OH stretching vibration, when the electric vector of the IR beam is parallel to the c-axis of the hexagonal structure; the OH line shows a maximum height. This line is not observed when the electric vector is perpendicular to the c-axis. These data indicate that the OH^- ion is parallel to the c-axis (Reprinted from Ref. [7]. Copyright 1994. With permission from Elsevier)

8.3.2 Dichroism

Dichroism corresponds to the change in line intensities related to the polarization of the IR or Raman beams with respect to the crystallographic axis. It can be used when monocrystals are available with shapes and morphologies compatible with the techniques in use for spectra recording. The activities of the different vibrational modes in polarized IR and Raman can be determined using factor group theory. Conversely, dichroism can be used to determine the orientation of crystals in a material or a biological tissue. One of the most interesting examples is that of the orientation of OH^- groups in hydroxyapatites [7]. Early works on natural monocrystals of dahlite (a carbonated hydroxyapatite) have shown that OH^- groups are parallel to the c-axis of the hexagonal structure (Fig. 8.3). Conversely, this orientation can be used to determine the orientation of hydroxyapatite crystals in materials or biological tissues like dental enamel [26].

8.3.3 Data Computing

The actual techniques of vibrational spectra acquisition in general permit the recording of spectra of high quality with excellent resolution and signal/noise ratio. However, very frequently an intrinsic broadening persists, related to the substance itself. Many computing techniques have been proposed to improve spectral resolution and line identifications. The easiest ones are second derivative and FTIR self-deconvolution [11, 21, 27]. A drawback is an enhancement of sharp slope changes in the spectra, whereas broad lines remain mostly unchanged and a lowering of the signal on noise ratio. Second derivative changes considerably the aspect of the spectra. With self-deconvolution, the aspect of the spectra is

preserved, but spurious bands may appear in case of overdeconvolution [28]. These resolution enhancement techniques are often associated with curve-fitting procedures, extensively used nowadays for quantitative evaluations. However, these techniques are difficult to validate, and, very often, several solutions may appear for the same spectrum, which leads to some heterogeneity in the published reports [29, 30] with variable numbers of lines and assignments. The line shape is an important parameter in curve-fitting; however, no definitive rule can be provided, and the best fitting parameters might not always correspond to the most relevant ones from a physical-chemical point of view. Whenever possible, the peak fitting procedure and line assignments should be supported by other data involving, for example, isotopic substitution, chemical analyses, or correlation with other techniques such as solid-state NMR. Curve-fitting techniques lead to a peak area or integrated intensity allowing quantitative determinations. It is very difficult, in the case of solids, to use the absolute line intensities, and generally the results are given as intensity ratios in a given domain. These integrated intensity ratios are often considered to represent the molecular composition of a phase or the composition of a mixture of phases. However, line intensity ratios should not be confused with molecular or phase ratios. The molecular extinction coefficients between molecules in different environments or in different phases can be very different, and appropriate standardization curves are needed to determine a chemical composition.

Other elaborate techniques such as principal component analysis can be applied to collections of spectra to determine the individual components involved in the series [31]. However, this technique presupposes, implicitly, that discrete individual compounds with invariable line positions are involved and thus excludes the existence of apparent continuous band shifts often observed in solid solutions. Many other techniques are available, including specialized data treatment software combining chemometrics and spectroscopy.

8.4 Substituted Well-Crystallized Calcium Phosphates

Very often biological apatites and other calcium phosphates can incorporate substitution ions, and the corresponding spectra can be strongly altered. Thus, in addition to phase identification, vibrational spectroscopies also allow the identification of site occupancies in crystalline solids and interactions between species in close proximity.

8.4.1 Substituted Apatites and Their Solid Solutions

Several types of substituted apatites may be found, from simple solid solutions involving different cations in stoichiometric apatites to complex substitutions

involving coupled replacements and vacancies. The spectra interpretation, including line assignments, for substituted compounds is considered to derive from those for pure, non-substituted compounds. However, at the molecular level, the differences in mineral ion environments due to solid solutions may be perceived as disruptions in the crystal periodicity and as alterations in the vibrator environments and symmetry. Thus, there is some ambivalence in interpreting spectra of substituted apatites considering either the global crystallographic structure or the local environments of the vibrating species.

8.4.1.1 Cation-Substituted Stoichiometric Apatites

The spectra of cationic solid solutions can often be related to those of pure compounds. An illustrative example is given by strontium–calcium hydroxyapatites. In the series Ca_{10-x} Sr_x $(PO_4)_6$ $(OH)_2$, the phosphate and OH lines are shifted between those of the end terms; pure calcium and strontium hydroxyapatites. The infrared lines are globally shifted towards lower wavenumbers when a large, heavy cation replaces a smaller, lighter one. This phenomenon is often related to the unit cell volume and, indirectly, to the substitution ratio. The number of lines, however, remains consistent for all spectra of the series with that for a stoichiometric calcium or strontium hydroxyapatite. The shift of simple lines like the Raman ν_1 PO_4 (Fig. 8.4) can be linearly correlated to the substitution ratio, even if the distribution of cations between the two cationic sites of the structure is not homogeneous in this kind of substitution. Similar observations have been reported by Bigi et al. [32]. This behavior is not, however, always observed, and discrepancies have been reported for lead–calcium apatites, for example [33].

Line broadening is generally observed for substituted apatites, which increases progressively with the substitution rate, reaching a maximum at about half substitution and decreasing when approaching the end point. Line broadening is generally related to the irregularity of the atomic array, often referred to as lattice strain, although several causes may be involved [34]. As the substitution ratio increases, the disorder increases and is attested to by line broadening. At a low level of substitutions, a dissymmetry of the Raman ν_1 PO_4 line is clearly observed, suggesting a slight unresolved band shift.

The position and shape of the FTIR or Raman stretching OH vibration follows the same rules (not shown). When we look at the FTIR OH libration line, however, a large gap exists between the extremes of the solid solution (from 633 cm^{-1} for calcium hydroxyapatite to 535 cm^{-1} for strontium hydroxyapatite), and the shift is no longer progressive and linear but seems to correspond to new line formations which could be tentatively assigned to a change in the cationic environments of the OH species, as shown for the Ca_9 Sr_1 $(PO_4)_6$ $(OH)_2$ sample (Fig. 8.5), where two OH libration lines can be distinguished.

Interestingly, for other types of hydroxyapatites, for example, calcium arsenate hydroxyapatites, the position of the OH stretching and libration lines is close to those of calcium phosphate, suggesting that it is the cationic environment of the

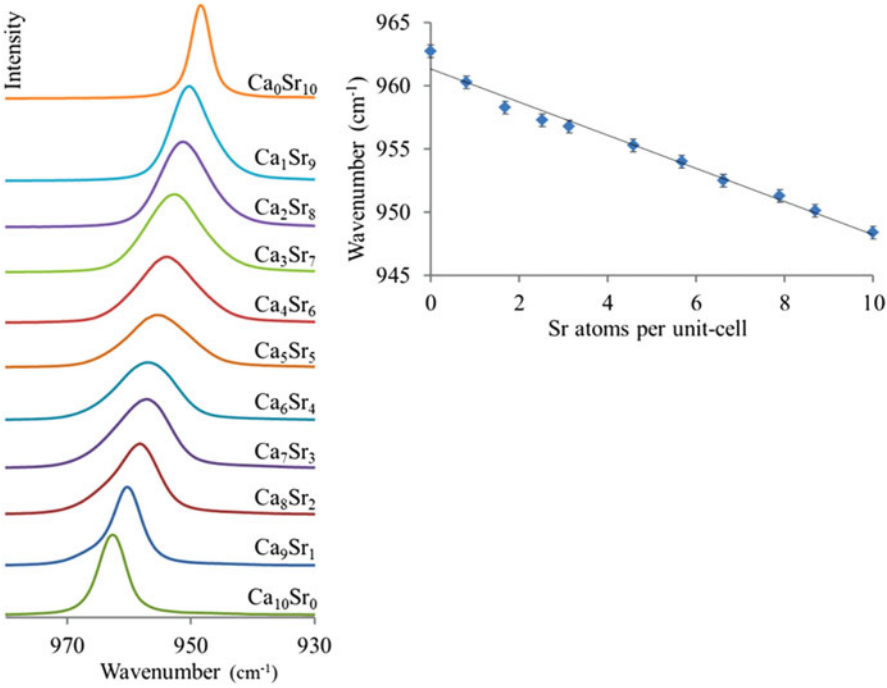

Fig. 8.4 Raman spectra of Sr–Ca hydroxyapatite solid solution in the ν_1 PO_4 domain and quasi-linear variation in the position of the Raman ν_1 PO_4 line as a function of the cationic composition

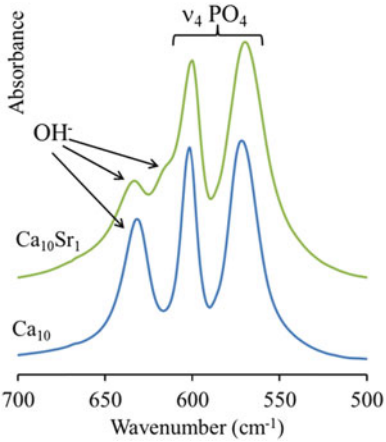

Fig. 8.5 FTIR spectra of OH^- libration line showing the formation of a second shifted OH^- line in Ca_9Sr_1 hydroxyapatite (2), in addition to the OH^- line of Ca_{10} hydroxyapatite (the assignment to the OH^- ion has been confirmed by deuteration, not shown)

OH^- ions that determines their vibrational and libration frequencies. The observation of several lines could then possibly be related to the local cationic environments of the OH vibrators and could potentially give information on clustering of cations in the apatite structure.

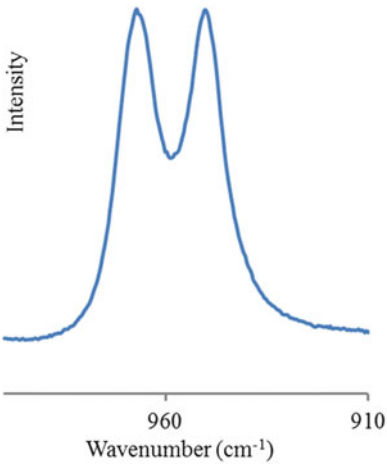

Fig. 8.6 Raman spectra in the ν_1 PO_4 domain of oxyapatite (with undetected OH^- line by Raman). The two lines at 966 and 951 cm^{-1} correspond to phosphate ions close to a O^{2-} ion or a vacancy

8.4.1.2 Substituted Anions and Nonstoichiometric Apatites

The replacement of phosphate ions in stoichiometric apatite by other ions like AsO_4^{3-} or VO_4^{3-}, for example, in lead fluorapatite, $Pb_{10}(PO_4)_{6-x}(VO_4)_xF_2$, induces an alteration in both molecular anion spectra, with a quasi-linear shift of lines relative to each anion, proportional to the substitution ratio, like in cation-substituted apatites [35]. This lines shift with the substitution ratio could probably be used to support the formation of a homogeneous solid solution.

The observation of the oxyapatite, Ca_{10} $(PO_4)_6$ O, spectra is interesting as it involves strong alterations in the infrared and Raman lines compared to its parent phase hydroxyapatite. The Raman ν_1 PO_4 line, for example (Fig. 8.6), is split into two components at 951 and 966 cm^{-1} which has been related to the formation of a vacancy in the monovalent anionic sites (OH^- sites) due to water release and the formation of O^{2-} ions [23]:

$$Ca_{10}(PO_4)_6(OH)_2 \rightarrow H_2O + Ca_{10}(PO_4)_6O \tag{8.1}$$

In oxyapatite, one half unit cell contains either a vacancy or an oxide ion corresponding to two kinds of local phosphate environments.

For a similar apatite, type A carbonate apatite, Ca_{10} $(PO_4)_6$ CO_3, also containing one bivalent anion and a vacancy per unit cell, the ν_1 Raman phosphate line is also split into two lines at 947 and 957 cm^{-1} [20].

Additionally, a general feature of this kind of apatite with a vacant anionic monovalent site is a rather specific phosphate line in the ν_3 PO_4 domain of the FTIR spectra at around 1,140 cm^{-1}. Such a line is observed, for example, in oxyapatite, type A carbonated apatite, sulfoapatite Ca_{10} $(PO_4)_6$ S, and peroxyapatite Ca_{10} $(PO_4)_6$ O_2 and has been related to the presence of bivalent ions and vacancies

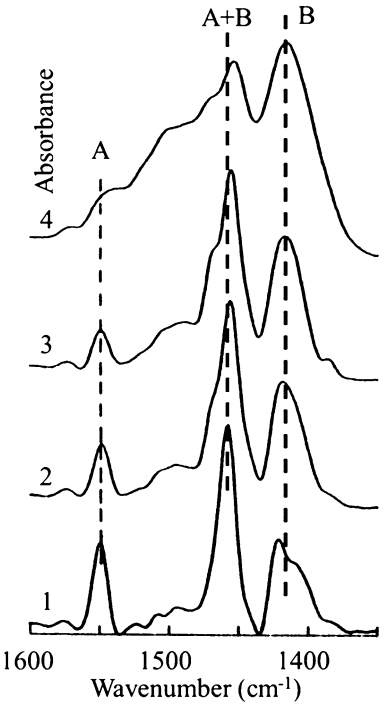

Fig. 8.7 Self-deconvoluted FTIR spectra in the ν_3 CO_3 domain of carbonate ions in mixed type AB carbonated apatites with increasing carbonate concentration (in weight %). 1–1.3 %; 2–2.8 %; 3–3.5 %; 4–10 %. At low concentrations, relatively thin lines can be seen for type A and B carbonate. As the concentration increases, new lines appear corresponding to interactions between carbonate species, and a line broadening associated with a loss of resolution is observed (Reproduced with permission from [37])

[36]. Interestingly, a line near this position is also observed in HPO_4^{2-}-containing apatites, which has been assigned in this case to a P–O stretching of HPO_4^{2-} ions in the apatite structure. It should be observed, however, that these apatites, like type B carbonated apatites (carbonate ions substituting phosphate ions), are considered to contain OH^- vacancies [7]. However, the 1,140 cm^{-1} line is not detected in type B carbonated apatites.

Another alteration observed in the spectrum of oxyapatite is an enhancement of the ν_2 PO_4 line compared with other apatites, which has not yet received a definitive explanation.

Among illustrative examples of substituted apatites are type AB carbonate apatites containing carbonate species replacing both the phosphate ions (type B) and hydroxide ions (type A) of hydroxyapatite: $Ca_{10}(PO_4)_{6-x}(CO_3)_x(OH)_{2-x-2y}(CO_3)_y$ [37]. At very low carbonate content, the carbonate species are dispersed in the crystals, and relatively thin and well-resolved carbonate bands can be observed (Fig. 8.7). This is generally the case when low amounts of substituents are used. When the carbonate concentration increases, the lines become broader, as expected in solid solutions, and, interestingly, new lines appear that have been attributed to interactions between carbonate species [37, 38] and also to the effect of coupled substitution like Na–CO_3 for Ca–PO_4, for example [39].

8.4.2 *Other Substituted Calcium Phosphates*

A few other examples of FTIR or Raman investigations of other substituted calcium phosphates have been proposed. Quillard et al., for example, have shown that the spectra of sodium- and potassium-containing β-TCP could be interpreted in a quantitative manner by evaluating the line intensities related to the alteration in the phosphate environments produced by this substitution [40].

8.5 Nanocrystalline Biomimetic Apatites

Nanocrystals are characterized by a very high surface area, and vibrational spectroscopies can be used to get information on the surface species. Several reports have been published revealing specific features considering nanocrystalline apatites of biological origin as well as synthetic biomimetic apatites [41, 42].

8.5.1 *Surface Characteristics of Biomimetic Nanocrystalline Apatites*

An interesting set of data is the comparison of FTIR spectra obtained on freshly precipitated nanocrystalline apatites in either the wet or dry state (Fig. 8.8) [43]. As water strongly absorbs IR radiation, such spectra are obtained either by using the attenuated total reflectance (ATR) technique or more simply by transmission through a thin layer of a suspension deposited on a polyethylene membrane. The data show that the spectra in the ν_1, ν_3 phosphate domain differ strongly.

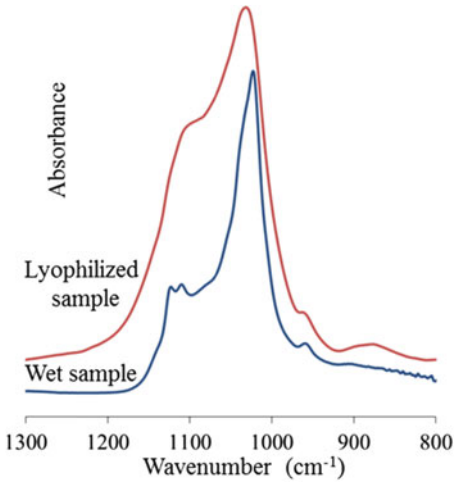

Fig. 8.8 FTIR spectra of biomimetic nanocrystalline apatites in the ν_1, ν_3 PO_4 domain: in a wet state (transmission through a thin layer on polyethylene); after freeze-drying (in a KBr pellet)

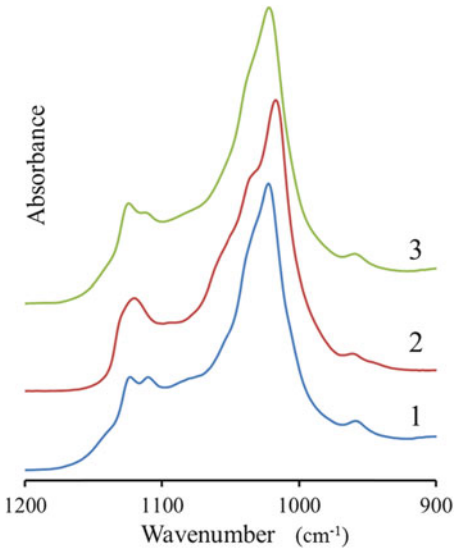

Fig. 8.9 FTIR spectra of biomimetic apatites in a wet state: *1* original sample; *2* sample 1 exchanged in a NH_4HCO_3 solution (1 M) for 5 min; *3* sample 2 exchanged back for 5 min with a 1 M $(NH_4)_2HPO_4$ solution. Illustration of the alteration related to carbonate ion uptake and the reversibility of the surface ion exchange (Reproduced with permission from [43])

In the wet state, relatively narrow lines are obtained, whereas in the dry state, a loss of resolution and band broadening are observed. The transition appears progressively on drying, and it has been assigned to the existence of a structured hydrated layer on the surface of these nanocrystals, which is destroyed upon drying leaving amorphous-like domains. When carbonate is present, such a hydrated layer with relatively thin spectral lines can also be observed, although with less clarity. Interestingly, ion exchanges, which can be easily realized, alter the structure of the hydrated layer, but these changes are reversible and the original features can be reestablished by reverse exchange reactions (Fig. 8.9).

At this point it should be recalled that vibrational spectroscopies are sensitive to local environments and surface environments can be very easily modified. Thus, the observation of an amorphous-like structure using vibrational spectroscopies does not necessarily mean that there is an amorphous phase precursor to the apatite formation. The example above shows that amorphous domains may form on the surface of existing nanocrystals but these do not constitute an isolated phase with defined boundaries, as would be the case with a precursor phase.

Considering the structure of the hydrated layer, FTIR shows that carbonate-free layers are close although not identical to OCP environments as predicted by Brown [44]. For the carbonated hydrated layer, we did not find three-dimensional model structures with comparable spectroscopic characteristics.

From ion exchange experiments, the characteristics of surface carbonate species can be determined (Fig. 8.10), either in the wet state or after drying and amorphization [43]. If the dried sample shows line positions and shapes analogous to those of amorphous calcium carbonate, distinct bands positions can be seen on wet samples, demonstrating again the role of water in the spectroscopic characteristics of surface species.

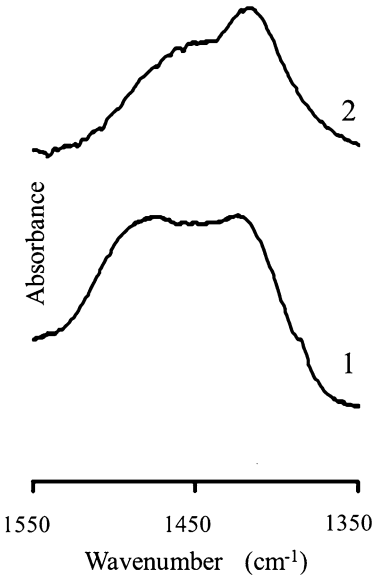

Fig. 8.10 FTIR spectra of biomimetic nanocrystalline apatites with surface carbonate ions in the ν_3 CO_3 domain: *1* after freeze-drying (in a KBr pellet); *2* in the wet state (transmission through a thin layer on polyethylene) (Reproduced with permission from [43])

8.5.2 Characterization of Nanocrystalline Apatites Using Isotopic Substitution

Isotopic substituted molecular ions can be incorporated as molecular probes into a material to follow alterations in their environments or chemical reactions. These can be used, for example, in apatite nanocrystals to identify sites of carbonate incorporation and alterations in the nanocrystals upon aging.

8.5.2.1 Surface Carbonate in Biomimetic Nanocrystalline Apatites

^{13}C carbonate is easily available and can be used to follow the carbonate species in exchange reactions involving the hydrated layer. When a ^{13}C carbonate-containing solution is put in contact with a ^{12}C carbonated nanocrystalline apatite, a surface equilibration occurs. The FTIR spectra were analyzed in the ν_2 CO_3 domain (Fig. 8.11). The isotopic shift is large enough in this domain to completely separate the ^{12}C and ^{13}C carbonate bands. The data show that the ^{12}C carbonate spectrum is mainly composed of thin lines at 879 and 871 cm^{-1}, respectively, assigned to type A and B carbonate. After contact with the ^{13}C carbonate-containing solution, the ^{13}C domain shows a broad line, characteristic of surface "amorphous" carbonate, without signs of ^{13}C carbonate incorporation in the apatite sites. The ^{12}C species present in the apatite domains are not modified by the ^{13}C carbonate solution treatment. The ^{13}C carbonate uptake is associated with a decrease in surface HPO_4^{2-} ions detectable by FTIR [45], consistent with a surface ion exchange.

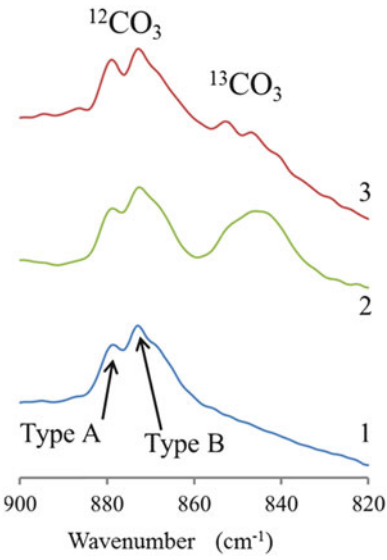

Fig. 8.11 Self-deconvolved FTIR spectra in the ν_2 CO_3 domain: *1* original precipitated ^{12}C carbonate apatite matured for 1 day; *2* original apatite 1 treated in 1 M ^{13}C carbonate solution for 20 min; *3* apatite 2 exchanged in 1 M HPO_4^{2-} solution for 20 min. All samples were freeze-dried after washing

It is possible to exchange back the surface ^{13}C carbonate in a second reaction, with HPO_4^{2-} ions (Fig. 8.11; spectrum 3); the data show that only the ^{13}C surface species have been removed and that once again the apatite's ^{12}C type A and B carbonate remains unchanged. Very faint lines corresponding to apatite carbonate type A and type B are seen in the ^{13}C domain, corresponding to a very small uptake of surface carbonate into the growing apatite domains, due to the brief maturation process taking place during the time of the exchange reaction.

These experiments clearly show the existence of two domains for the carbonate ions inside the nanocrystalline apatite domains (type A and B carbonates) that are stable and nonreactive and on the surface of these domains, comprising a hydrated layer in which carbonate ions can be easily trapped.

8.5.2.2 Maturation Process

Solution exchanges can also be used to pursue the incorporation of carbonate species during aging into nanocrystalline apatites, which is also referred to as maturation.

In these sets of experiments, the nanocrystalline apatites were first precipitated into a ^{12}C or a ^{13}C carbonate-containing solution. After different periods of aging, the solutions were exchanged and the ^{12}C carbonated samples were separated and put in ^{13}C carbonate solutions and vice versa. The spectra obtained after recovering and freeze-drying the samples were analyzed in the ν_2 CO_3 domain. The data are shown only for the ^{13}C-precipitated and then ^{12}C-treated samples (Fig. 8.12).

The samples corresponding to solution substitution at time 0, immediately after precipitation, contain essentially all ^{12}C carbonate. When the solution exchanges

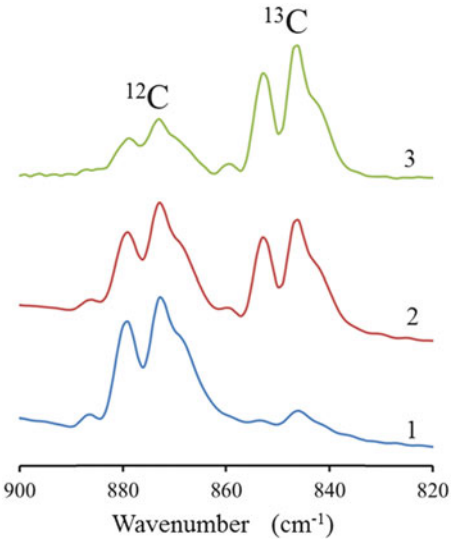

Fig. 8.12 Self-deconvoluted FTIR spectra in the ν_2 CO_3 domain of apatites prepared in a ^{13}C carbonate-containing solution (1 M) matured for different times and put in ^{12}C carbonate solution for 3 additional weeks. *1* initial maturation time 0 in the ^{13}C precipitation solution, most carbonate species are incorporated as ^{12}C during the 3 weeks after the solution exchanges; *2* 3 days maturation in the ^{13}C solution before the exchange; *3* 9 days maturation in the ^{13}C solution before the exchange. The ^{13}C carbonate line intensity increases progressively as the initial maturation time increases, whereas the ^{12}C carbonate line intensity decreases (Reprinted from Ref. [45]. Copyright 2007. With permission from Elsevier)

occur later after precipitation, however, the proportion of ^{13}C carbonate increases and that of ^{12}C carbonate decreases. The first noteworthy observation is that the carbonate ions are incorporated in these nanocrystalline apatites during aging and that they are not trapped in the apatite domains during the fast precipitation. The carbonate taken up during precipitation exists essentially as easily exchangeable surface carbonate. The second observation is that the ratios between type A and type B locations do not vary significantly with time of uptake during aging and that species already in the apatite domain are not altered. The third phenomenon revealed by these experiments is that the ability to incorporate carbonate ions slows down considerably with time reflecting a loss of reactivity of the nanocrystals on aging related to the decrease of proportion of the unstable surface hydrated layer which nourishes the growth of the apatite domains.

The comparison of apatites precipitated in $^{13}CO_3$ solutions, aged for 3 days, then treated in $^{12}CO_3$ solutions with symmetrical samples precipitated in $^{12}CO_3$ solutions and aged for 3 days, and then treated in $^{13}CO_3$ solutions (Fig. 8.13) indicates, in addition, that the line resolution is always better for the first carbonate species to enter ($^{13}CO_3$ and $^{12}CO_3$, respectively), which can be interpreted as an improvement in the local organization possibly related to the growth of the apatite domains at the expense of the unstable hydrated surface layer.

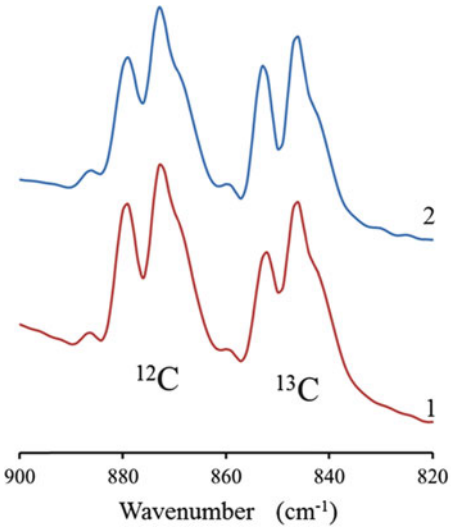

Fig. 8.13 Deconvoluted spectra in the ν_2 CO_3 domain of: *1* apatites precipitated in the ^{12}C carbonate-containing solution matured for 3 days and put in ^{13}C carbonate solution for 3 additional weeks and *2* apatites precipitated in the ^{13}C carbonate-containing solution matured for 3 days and put in ^{12}C carbonate solution for 3 additional weeks. The first trapped carbonate species are more resolved and correspond to their environments with better crystallinity (Reprinted from Ref. [45]. Copyright 2007. With permission from Elsevier)

8.6 Examples of the Use of Vibrational Spectroscopies in Biominerals and Biomaterials Involving Calcium Phosphates

8.6.1 Plasma Sprayed Coating

Plasma spraying of hydroxyapatite (HA) is largely used to improve the biological activity and biointegration of orthopedic metal implants [46–48]. However, it is well established that HA decomposes during plasma spraying, leading to the formation of different phases [48–50]. This reported decomposition has several advantages and drawbacks for the behavior of the coatings after implantation. Plasma sprayed coatings are mainly composed of crystalline HA and oxyapatite (OA) embedded into a relatively soluble amorphous phase (ACP). Sometimes CaO, TTCP, and α- or β-TCP are also present, generally in small proportions. In order to determine the material's quality, several standards have been published regarding the coating's chemical composition (Ca/P ratio), phase composition, and crystallinity (ISO 13779-3:2008). Most of these characterizations are based essentially on X-ray diffraction (XRD) analyses. However, several additional parameters that are more difficult to determine, such as the main phase proportions and their distribution within the coating and more specifically the amount of amorphous phase, are not considered in the standards, although they could be related to the coating behavior in vitro and in vivo. All the phases detected in a plasma sprayed coating can theoretically be distinguished by Raman spectroscopy, especially the most important, in some instances with better sensitivity than by XRD. In addition, Raman scattering allows local investigations of the coating's heterogeneity [50–53].

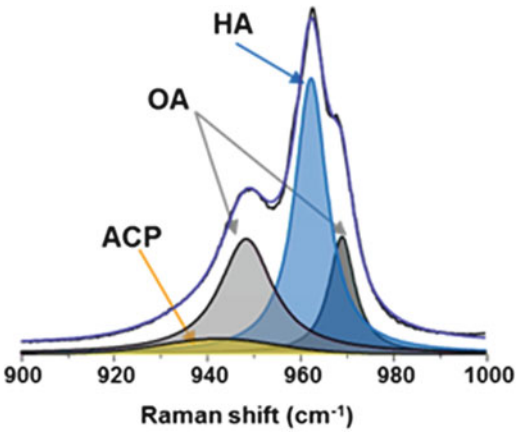

Fig. 8.14 Raman spectra of plasma sprayed coating in the ν_1 PO_4 domain showing the main phases: amorphous calcium phosphate (ACP), oxyapatite (OA), and hydroxyapatite (HA) (Reprinted from Ref. [54]. Copyright 2012. With permission from Elsevier)

Micro-Raman imaging based on different representations from the same data set may provide a powerful means to study structural alterations and visualize the distribution of phases within heterogeneous plasma sprayed HA coatings. The $\nu_1 PO_4$ domain, with strong thin lines, seems well adapted for imaging (Fig. 8.14) [54]. The ACP especially is characterized by a broad Raman line around 950 cm^{-1}, and all crystalline phases show lines distinct from that of apatite at 961 cm^{-1}. The OA, so difficult to distinguish by other methods, exhibits very specific Raman scattering lines at about 951 and 966 cm^{-1}, as mentioned earlier [23]. CaO is the only phase that cannot be detected in this domain.

An accurate mapping of the different phases in HA coatings can be obtained by micro-Raman imaging involving curve-fitting in the ν_1 PO_4 domain, extraction of the characteristic line(s) associated with specific phases, and of their relative intensities. It should be noticed that at this stage, without accurate standardization, the data represent only the relative integrated intensities of lines associated with a specific phase and their relative variation, but not their real content in the coating. In the example shown in Fig. 8.15, we can see the distribution of the HA, OA, and ACP in a cross section of a coating obtained using a low-energy plasma spray device [54].

The domains rich in oxyapatite appear relatively narrow and dispersed. Two types of OA-rich domains can be distinguished, those found within the amorphous phase, which may correspond in part to a recrystallization process, and those contiguous to HA domains, possibly formed by dehydration during the particles' flight. HA-rich domains might correspond to solid particle cores. It clearly appears that HA-rich domains exist in zones with low amorphous content.

In addition to a heterogeneous distribution of phases through the thickness of the deposit, there is also a heterogeneous distribution on its surface, and very different Raman spectra are collected depending on the location [55]. Therefore, Raman microspectroscopy can be used as a routine nondestructive tool to obtain rapid analysis of the composition of apatite coatings and even of different domains

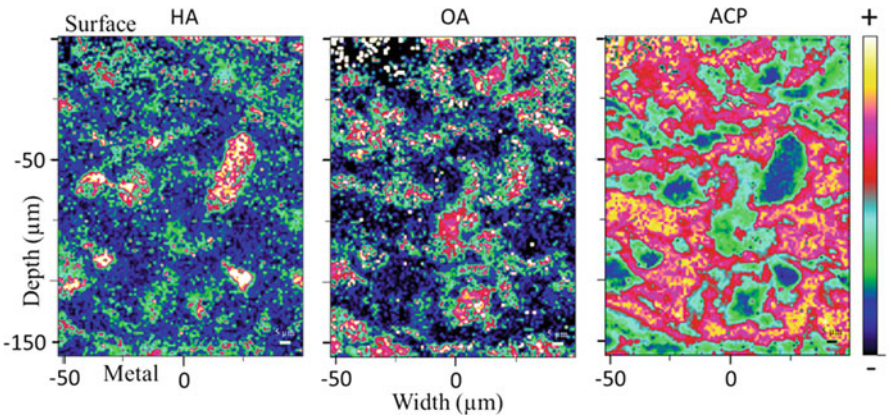

Fig. 8.15 Raman mapping of the main calcium phosphate constituents in a cross section of a plasma sprayed coating obtained using a low-energy mini-torch [55]. Relative areas of specific lines: HA, hydroxyapatite (962 ± 1 cm^{-1}); OA, oxyapatite (957 ± 1 cm^{-1}); and ACP, amorphous calcium phosphate (948 ± 2 cm^{-1}). The amorphous phase appears as a binder. Islands of HA are surrounded and superimposed to OA. HA is never totally absent suggesting a recrystallization from the amorphous phase

of a splat. This technique could be adapted for the chemical characterization of the coating directly on biomedical implants. Image analyses could then be used to describe the coating characteristics with accuracy.

8.6.2 Setting Reactions of Calcium Phosphate Cements

Calcium phosphate cements have been widely used as bone substitute materials since the 1980s, and generally FTIR and Raman spectroscopy are involved in the characterization of the set cements. Interestingly, this technique can also be implemented to study the cement paste composition during setting and hardening and thus provides kinetics data on the chemical reaction(s) involved during these processes. Generally it is only the physical setting that is examined according to standards.

Two methods can be used for such a study: (1) lyophilization of cement paste after different maturation periods (water removal stops the chemical reaction) and then preparation of a KBr pellet of the sample for transmission mode FTIR analysis and (2) direct real-time FTIR analysis of cement paste using a horizontal attenuated total reflectance device equipped with a standard ZnSe monocrystal [56]. This technique allows direct follow-up of the cement setting reactions and kinetics. We present herewith an example of this kind of FTIR analysis on vaterite $CaCO_3$–dicalcium phosphate dihydrate (DCPD) mixed cement to study the influence of a solid phase co-grinding treatment on the cement setting reaction [57].

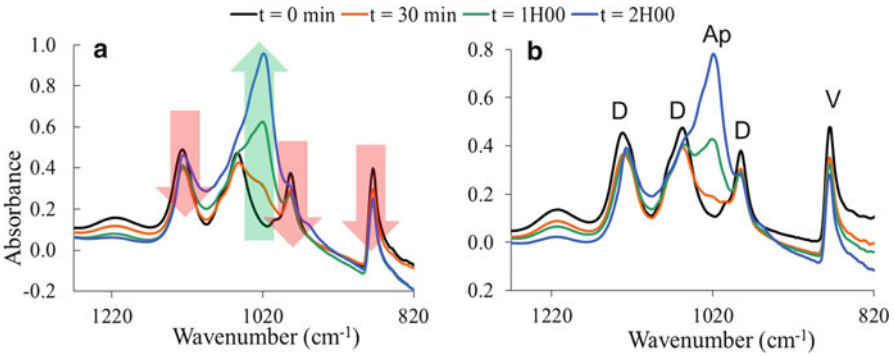

Fig. 8.16 Real-time evolution of the FTIR spectra of a cement paste at 37 °C: (**a**) the cement paste prepared with unground solid phase; (**b**) the cement paste prepared with co-ground solid phase (*D* DCPD, *V* vaterite, *Ap* apatite) (Reproduced with adaptation from Ref. [56]. Copyright 2011. With permission from Elsevier)

It has previously been shown that the setting reaction of the reference cement is based on the chemical reaction of DCPD on vaterite, leading to a solid form composed of nanocrystalline carbonated apatite analogous to bone mineral associated with untransformed vaterite $CaCO_3$.

Hydrogen phosphate groups in brushite (at 985, 1,058, 1,132, and 1,222 cm^{-1}), phosphate groups in apatite (at 1,020 cm^{-1}), and carbonate groups in vaterite (at 876 cm^{-1}) can be identified by FTIR spectroscopy. We focused on examination of modifications in the phosphate and carbonate domains of the spectrum.

Figure 8.16a illustrates the setting reaction of a reference cement paste: a decrease in the brushite and vaterite lines is associated with an increase in the apatite lines. Figure 8.16b shows the evolution of the FTIR spectrum (in the range 1,270–820 cm^{-1}) of a cement paste made of previously co-ground brushite and vaterite powders. Significant differences can be seen regarding the progression of the setting reaction, especially during the first hour of paste evolution [56]. Interestingly, 30 min after paste preparation, the intensity of the band (shoulder) at 1,020 cm^{-1} characteristic of apatite is lower in the case of the co-ground cement than in the case of the reference cement. This marked difference in 1,020 cm^{-1} band intensity is also visible if we compare spectra obtained after 1 h (Fig. 8.16a, b), thus indicating a significant effect of co-grinding on cement setting reaction kinetics. This effect is also marked when comparing the decrease in intensity of the weak phosphate band of DCPD at 1,222 cm^{-1} for both cements: a delay in the decrease in intensity of this band is noted for the cement paste prepared with a co-ground solid phase, especially if we compare spectra corresponding to 1 h of cement paste evolution (Fig. 8.16a b).

This kind of study can easily be transposed to other systems and allow a convenient and precise evaluation of the effect of additives, pretreatments, or impurities on cement setting and hardening reactions.

8.6.3 Adsorption of Biomolecules and Drugs

Bioactive molecules often exhibit a high binding affinity for calcium phosphate surfaces through ionic end groups. Adsorption properties of apatites are involved in biological molecule chromatography and in the regulation of biological processes like biomineralization [58–60]. In the biomaterials field, adsorption of drugs on apatitic surfaces can be used to confer a therapeutic activity to substitutive biomaterials based on calcium phosphate [61]. FTIR and Raman spectroscopies appear to be powerful tools in understanding the interactions of bioactive molecules with apatitic surfaces; they have been widely utilized, for example, to study bisphosphonate adsorption on apatite in vitro [62, 63] or, potentially, in vivo, using surface-enhanced Raman spectroscopy (SERS) [64]. Bisphosphonate molecules (BPs) are used as successful antiresorptive agents for the prevention and treatment of bone diseases such as osteoporosis. They present a high affinity for apatitic surfaces and prevent mineral dissolution and bone resorption, inhibiting osteoclast activity [65]. The adsorption equilibrium of such drugs with apatitic surfaces can be described by a Langmuir isotherm, and follow-up of the variation in the mineral ion content of the solution after adsorption indicates that the adsorption reaction can be described as an ion exchange process between phosphonate groups of BPs molecules in solution and phosphate groups on the apatitic surface [66].

Raman microspectroscopy provides a powerful way to acquire information about chemical composition at a molecular level, even in aqueous environments. Moreover most BP molecules contain aromatic or conjugated domains and are therefore strong Raman scatterers. For example, considering the Raman spectra of biomimetic apatitic nanocrystals after adsorption of a bisphosphonate, tiludronate (Fig. 8.17), several vibration bands attributable to tiludronate are observed.

Some of them, especially those of phosphonate groups, are hidden by those from phosphate ions of the substrate. However, additional lines appear at 745 and 1,575 cm^{-1} corresponding to C–S and aromatic ring chain vibrations, assigned to tiludronate. Thus, the spectroscopic data from adsorbed molecules permits to confirm the presence of BPs on apatitic supports, and the irreversibility of such adsorption processes on solution diluting or sample washing [67]. Quantitative determinations can be performed directly on such systems, and a linear variation is obtained for the line area ratio of 746 or 1,575 cm^{-1} lines of tiludronate on the 961 cm^{-1} phosphate line of apatite (Fig. 8.17). These determinations could be improved using statistical analysis and chemometric methods.

8.6.4 Near Infrared Spectroscopy

Near infrared spectroscopy (NIR) may also be considered as an interesting complementary tool for physicochemical characterizations, for example, where the analysis of adsorbed water molecules is concerned. Indeed, water absorption bands in the NIR region (composed of combination transitions and overtones, [68]) are

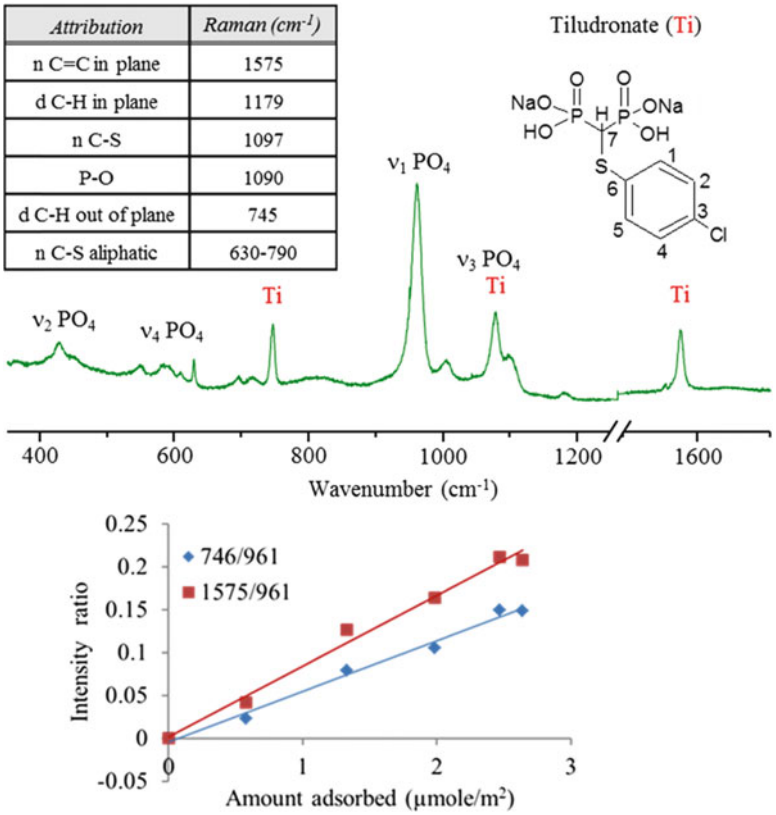

Fig. 8.17 Raman spectrum of a biomimetic nanocrystalline apatite after adsorption of tiludronate and variation of the intensity ratio of tiludronate lines at 746 and 1,575 cm^{-1} on the ν_1 PO_4 apatite line at 961 cm^{-1} [67]

characterized by weaker extinction coefficients than in the mid-IR region where the absorption due to water molecules can approach saturation, especially for samples exhibiting a high surface area. NIR analyses have, for instance, been exploited to explore surface hydration phenomena on nanocrystalline apatite samples, including surfaces with cationic substituent such as Mg^{2+} ions [69]. In this type of experiment, some biomimetic samples (preliminarily outgassed at room temperature) were equilibrated with water vapor and analyzed by NIR in situ, to follow interaction phenomena with surface water molecules.

NIR absorption bands due to water molecules in the 6,800–7,200 cm^{-1} range may be overlapped by harmonic vibrations of apatitic OH^- ions; therefore, attention can be focused on the more specific $\delta + \nu_{asym}$ combination mode of water molecules located at lower frequencies, in the 5,500–4,500 cm^{-1} region: this mode was indeed shown to be rather sensitive to hydrogen bonds involving water molecules, leading to a variety of NIR contributions due to molecules experiencing different types of interactions with the surface [68, 70].

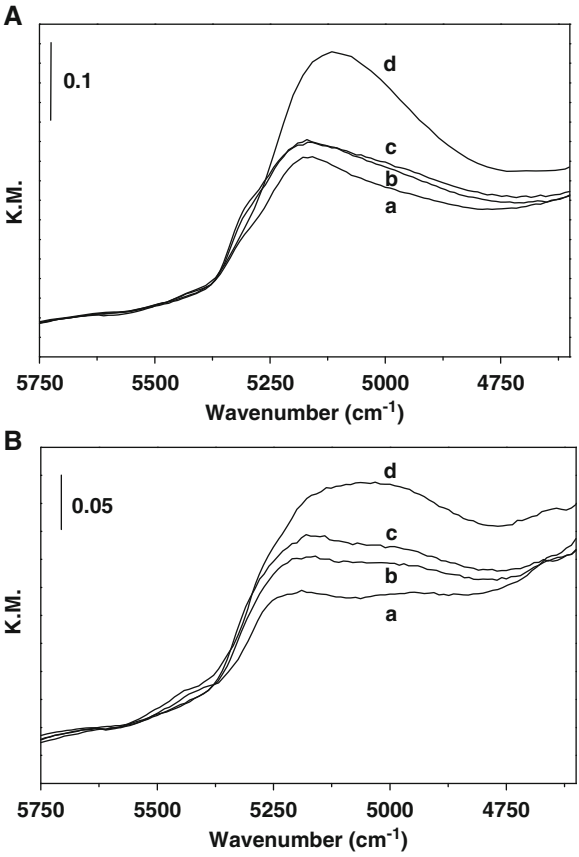

Fig. 8.18 NIR spectra in the 5,750–4,720 cm^{-1} range of nanocrystalline apatite (nap). Panel **A**: samples in contact with water vapor: line a- nap at 1 day maturation; line b- nap-1d with 0.9 % Mg on the surface obtained by ionic exchange; line c- nap-1d with 1.3 % Mg; line d- nap-1d with 3.0 % Mg (d). Panel **B**: samples after outgassing at room temperature for 1 h (Reprinted from Ref. [69]. Copyright 2009. American Chemical Society)

The $\delta + \nu_{asym}$ H_2O band for water adsorbed on nanocrystalline apatite [69] (Fig. 8.18A, line a) was found to be multicomponent in nature, with a main absorption around 5,170 cm^{-1}, attributed to H_2O molecules acting as donors of two equivalent H bonds, and two shoulders at about 5,300 (narrow) and 5,000 (broad) cm^{-1} attributed to the OH moieties (non H-bonded and H-bonded, respectively) of water molecules acting as donors of a single H bond [68, 69, 71]. The presence of water molecules in direct contact with the crystal's surface, as well as water overlayers, was assumed. The introduction of Mg^{2+} ions by way of Ca^{2+}/Mg^{2+} surface exchanges in solution was found to result in an increased overall intensity in the $\delta + \nu_{asym}$ H_2O band (Fig. 8.18A, lines b and c), unveiling additional water adsorption capabilities for Mg-enriched samples. NIR spectroscopy thus suggested that apatite samples enriched with Mg^{2+} retained more water at their surface than Mg-free counterparts. Although the increase in the amount of adsorbed water did not appear to be strictly proportional to the Mg^{2+} content, the ion distribution on the surface of the nanocrystals is bound to vary upon Mg enrichment, and these findings may be linkable to the greater interaction of Mg^{2+} ions with H_2O molecules as compared to Ca^{2+}.

The residual $\delta + \nu_{asym}$ pattern found after contact with water vapor and subsequent outgassing at room temperature (thus solely representative of "irreversibly" adsorbed water molecules) was also investigated [69]. The related NIR absorption profile then mostly exhibited two partially overlapped components at ca. 5,190 cm^{-1} and ca. 4,950 cm^{-1} (Fig. 8.18B, line a). In the case of samples enriched with Mg^{2+}, a broad component appeared in the range 5,150–5,000 cm^{-1}. In all these cases, the absence of high-frequency components suggested that both O–H groups from "irreversibly" adsorbed H_2O molecules were probably involved in hydrogen bonds.

Such NIR findings thus illustrate the coexistence of various types of adsorbed water on nanocrystalline apatites (as witnessed by changes in relative intensities and positions), and the nature of surface cations (e.g., Ca^{2+}, Mg^{2+}) was shown to have a direct effect on water adsorption capabilities. These modifications are, however, probably not limited to water molecules in direct contact with the surface (Fig. 8.18B) but could also involve water overlayers (Fig. 8.18A).

8.6.5 Pressure Effects and Residual Strains

Vibrational energy levels are sensitive to pressure exerted on crystals, and they offer an interesting ability to detect residual strains. Generally when a sufficiently high pressure (on the order of several GPa) is applied to a crystal, the FTIR or Raman lines are shifted to higher wavenumbers as shown in the case of fluorapatite $Ca_{10}(PO_4)_6F_2$ (Fig. 8.19) [71].

Shifts towards lower wavenumbers are also possible and have been reported for water molecules and for ions involved in strong hydrogen bondings [73]. The increase in pressure is also associated with line broadening and a loss of resolution. In several cases phase transitions under pressure have been reported. The observed shifts ($d\nu$) are proportional to the applied stress (dP), and the slopes ($d\nu/dP$) have been reported for some calcium phosphates (Table 8.8) [72–74]. The $d\nu/dP$ values depend on the vibrational mode and may vary considerably, as for monetite, for example, where the negative value reported for the 1,070 cm^{-1} line is attributed to strong hydrogen bonding involving the HPO_4^{2-} ions. Very similar values are observed for the ν_1 lines of apatite samples. When pressure initiates a phase transition, $d\nu/dP$ variations generally show a discontinuity.

There are only a few studies involving solid solutions such as carbonated apatites [75, 76]. In their study of type B carbonate apatite and bone mineral, de Carmejane et al. [75] showed that $d\nu/dP$ was much higher for the ν_1 phosphate line than for the ν_1 carbonate line. They attributed this difference to the greater rigidity of carbonate ions compared to phosphate. In all cases the alterations of the spectra under isostatic pressure were found to be reversible and disappeared when the pressure was released.

Several authors have claimed that it was possible to determine residual strains in several cases, in coatings and in bone mineral, for example. In both cases, however,

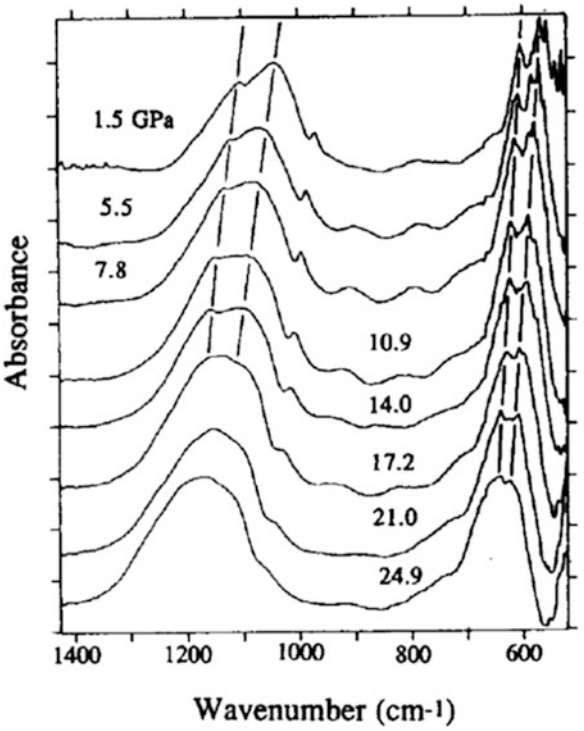

Fig. 8.19 FTIR spectra of fluorapatite submitted to different pressures, showing the line shifts towards higher wavenumbers (Reprinted from Ref. [72]. Copyright 1996. With permission from Elsevier)

Table 8.8 Infrared line shifts as a function of the applied pressure: $d\nu/dP$ ($cm^{-1}.kbar^{-1}$) for different representative lines of calcium phosphates in the ν_1, ν_3 domain, at room temperature

Compound	Line position without pressure (cm^{-1})	$d\nu/dP$ Low-pressure phase	$d\nu/dP$ High-pressure phase
$Ca_{10}(PO_4)_6F_2$ fluorapatite (FA)	1,095 (ν_3)	0.56	–
	964 (ν_1)	0.42	–
$Ca_{10}(PO_4)_6(OH)_2$ hydroxyapatite (HA)	1,089 (ν_3)	0.58	0.06
	1,033 (ν_3)	0.46	0.06
	963 (ν_1)	0.41	0.08
$CaHPO_4$ monetite (DCPA)	1,132 (ν_3)	0.26	
	1,070 (ν_3)	−0.11	
	996 (ν_1)	0.29	
$CaHPO_4$, $2H_2O$ brushite (DCPD)	1,141 (ν_3)	0.64	0.50
	1,066 (ν_3)	0.31	0.27
	998 (ν_1)	0.48	0.34

the line displacements observed could be due to the existence of solid solutions with different compositions. In the case of bone [77], the Raman spectra at a zone indented with a cylindrical indenter were analyzed using multivariate factor analysis. The data revealed that additional mineral factors appeared in the floor of

the indent. These new factors were attributed to pressure alterations in the mineral phase. It should be noted that these alterations appeared at relatively low pressures (0.4–1.2 GPa) compatible with physiological loadings. The possibility of obtaining permanent alterations, though the effect of pressure was found to be reversible, has been related to the difference between an isostatic pressure, preventing ion and water displacement, and axial loading. The organic matrix was found to be affected near the indent edge. The new factor appearing there was assigned to a loss of the collagen triple helical structure resulting in a disordered state of the protein related to a rupture of cross-links. Similar observations have been published related to fatigue microdamage in bone [78].

8.6.6 Orientation of Crystals

The orientation of apatite crystals in biological tissues has often been studied by electron micro-diffraction. Although Raman and FTIR spectroscopies can also be used to determine crystal orientation, the spatial resolution of FTIR is too broad to analyze crystals with small sizes and can only give information on collections of crystals in textured domains. Micro-Raman spectroscopy offers a unique tool for assessing the orientation of crystals within rather small domains of a few μm^3, with some constrains due to the use of common optics on a single axis for both the excitation and the scattered beam [79]. Micro-Raman spectroscopy has been used for the determination of crystal orientations in tooth enamel and in bone. In enamel, comprised of well-crystallized apatites and exhibiting a well-resolved Raman spectrum, clear data can be obtained on specifically identified lines, and the apatite crystals have been found to be oriented with the c-axis of the hexagonal structure perpendicular to the tooth surface [25]. In bone the spectral resolution is lower and lines are superimposed. In addition, the orientation of crystals has to be compared to that of collagen fibers, which vary within an osteon and even a lamella. The data are presented mainly as variations in intensity ratios of chosen lines of the collagen matrix and the mineral [80]. An angular dependence of the spectra of the collagen matrix and bone mineral can be detected, indicating orientation correlations (Fig. 8.20). Using these correlations, variations in the orientation of crystals could be detected within an osteon lamellae using polarized Raman microscopy.

8.6.7 Maturity and Crystallinity of Bone Mineral

Bone mineral is a nanocrystalline apatite, and it evolves with age in a similar manner to synthetic biomimetic nanocrystalline apatites: the nanocrystals exhibit, just after their formation in early embryonic bone, a well developed hydrated

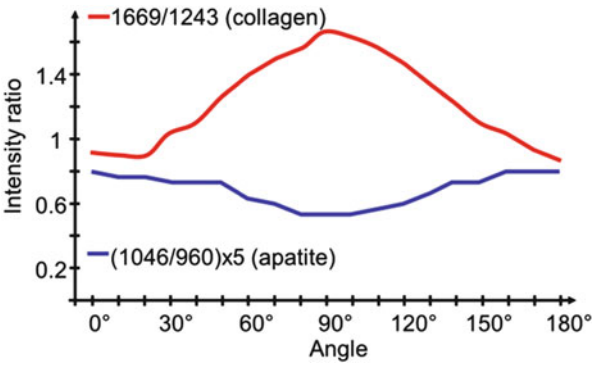

Fig. 8.20 Angular variations in the lines intensity ratios of bone Raman microspectra of an osteon lamella as a function of sample orientation with respect to the polarization of the incident beam. Collagen fibres: 1,669/1,243 cm^{-1}; apatite crystals: 1,046/960 cm^{-1} (Redraw from [80])

layer rich in HPO_4^{2-} and non-apatitic carbonate species [81]. Upon aging, this layer, which is thermodynamically less stable than apatite, is progressively replaced by stable apatite domains, and carbonate ions are progressively incorporated in the apatite domains. The precise characterization of bone mineral would then necessitate the determination of both the extension and the content of the hydrated layer and the apatite domain.

Maturation of bone mineral is related to its changes with age and is often associated with an improvement in the crystallinity of the apatite phase, first determined by X-ray diffraction [82]. Later spectroscopic methods using a specific ratio of phosphate bands were correlated to XRD determinations of apatite crystallinity [29, 31], and a certain confusion exists about the maturation and crystallinity of bone mineral. Maturity can be defined as the ratio between non-apatitic surface environments present in the hydrated layer of the bone crystals and apatite environments. Crystallinity is related to the size and strains of crystallized apatite domains and ignores the surface hydrated layer. Although in many cases these two parameters evolve concomitantly, this might not always be the case, as shown by the example of fluorotic bone [80], and a careful characterization of bone mineral should separate these two parameters. The crystallinity of the apatite domains can be determined by XRD; however, such determinations at a microscopic scale are difficult, and a crystallinity index can be obtained using the FTIR line broadening of the ν_4 apatite line at 600 cm^{-1}. A proposed maturity index is obtained by determining the ratio of the integrated intensity of a line at 1,030 cm^{-1} assigned to phosphate ions in the apatite domain, with that of a line at 1,110 cm^{-1} assigned to phosphate groups in non-apatitic domains [83]. The results on human bone compared to synthetic samples show a greater amount of non-apatitic environments in bone mineral and a poor correlation with the crystallinity index specifically related to the apatite domain as it is defined in this study. Although we are still far from complete knowledge of the content and proportion of apatitic and non-apatitic domains, this first approach confirms the importance of non-apatitic domains in bone mineral characteristics and their possible stabilization or renewal.

8.7 Conclusion

The use of vibrational spectroscopies for the characterization of calcium phosphates will continue to develop because of their several major advantages, including the possibility of reaching micrometric domains and the related imaging ability, the ease and rapidity of information recording, and their relatively low cost. One of the major advantages of these techniques is their ability to give very reproducible and accurate information on nanocrystalline calcium phosphates. Future developments will include analyses of line shapes and improvements in curve-fitting techniques in the case of solid solutions and ion interactions with the possibility, thanks to theoretical spectra predictions, of reaching inhomogeneities of ion distributions in the crystals. Other developments will include analyses of images and association with chemometric techniques. These techniques, which can easily be automated, will also permit unitary control of medical devices, each device being analyzed and provided with its own characteristics. The standards in use will have to take these developments into account and adaptations should follow. The techniques related to vibrational spectroscopies have evolved rapidly with ultrafast vibrational spectroscopy or multidimensional spectroscopy, opening new possibilities in material science and chemistry.

Acknowledgments We are grateful to Gérard Leroy for discussions regarding the content of this chapter, and we thank Imane Demnati, Solene Tadier, and Patricia Pascaud for allowing us to use the results of their Ph.D. thesis in Figs. 8.15, 8.16, and 8.17.

References

1. Bishop DM (1993) Group theory and chemistry. Dover Publications, New York
2. Ross SD (1972) Inorganic infrared and Raman spectra. McGraw-Hill, Maidenhead
3. Farmer VC (ed) (1974) The infrared spectra of minerals. Mineralogical Society, London
4. Santhyanarayana DN (2011) Vibrational spectroscopy. New Age International Publisher, New Delhi
5. Casciani F, Condrate RA Sr (1979) The vibrational spectra of brushite. $CaHPO_4{\cdot}2H_2O$. Spectrosc Lett 12:699–713
6. White WB (1974) The carbonate minerals. In: Farmer VC (ed) The infrared spectra of minerals Mineralogical society monograph, 4th edn. Mineralogical Society, London
7. Elliott JC (1994) Structure and chemistry of the apatites and other calcium orthophosphates. Elsevier, Amsterdam
8. Bertoluzza A, Battaglia MA, Bonora S, Monyi P (1985) Hydrogen bonds in calcium acidic phosphates by infrared and Raman spectra. J Mol Struct 127:35–45
9. Trpkovska M, Soptrajanov B, Malkov P (1999) FTIR re-investigation of the spectra of synthetic brushite and its partially deuterated analogues. J Mol Struct 480–481:661–666
10. Posset U, Löcklin E, Thull R, Kiefer W (1998) Vibrational spectroscopic study of tetracalcium phosphate in pure polycrystalline form and as a constituent of a self-setting bone cement. Biomed Mater Res 40:640–645
11. Markovic M, Fowler BO, Tung MS (2004) Preparation and characterization of a comprehensive hydroxyapatite reference standard. J Res Natl Inst Stand Technol 109:553–568

12. Fowler BO, Moreno EC, Brown WE (1996) Infrared spectra of hydroxyapatite octacalcium phosphate and pyrolysed octacalcium phosphate. Arch Oral Biol 11:477–492
13. Jillavenkatesa A, Condrate RA Sr (1998) The infrared and Raman spectra of α- and β-tricalcium phosphate ($Ca_3(PO_4)_2$). Spectrosc Lett 31:1619–1634
14. Fowler BO, Markovic M, Brown WE (1993) Octacalcium phosphate. 3. Infrared and Raman vibrational spectra. Chem Mater 5:1417–1423
15. Ulian G, Valdre G, Corno M, Ugliengo P (2013) The vibrational features of hydroxylapatite and type A carbonated apatite: a first principle contribution. Am Miner 98:752–759
16. Treboux G, Layrolle P, Kanzaki N, Onuma K, Ito A (2000) Symmetry of Posner's cluster. J Am Chem Soc 122:8323–8324
17. Yin X, Stott J (2003) Biological calcium phosphates and Posner's cluster. J Chem Phys 118:3717–3723
18. Petrov I, Soptrajanov B, Fuson N, Lawson JR (1967) Infrared investigation of dicalcium phosphates. Spectrochim Acta 23A:2636–2646
19. Penel G, Leroy G, van Landuyt P, Flautre B, Hardouin P, Lemaitre J, Leroy G (1999) Raman microspectrometry studies of brushite cement: in vivo evolution in a sheep model. Bone 25(suppl 2):81S–84S
20. Penel G, Leroy G, Rey C, Bres E (1998) Micro-Raman spectral study of the PO_4 and CO_3 vibrational modes in synthetic and biological apatites. Calcif Tissue Int 63:475–481
21. Walters MA, Leung YC, Blumenthal NC, LeGeros RZ, Konsker KA (1990) A Raman and infrared spectroscopic investigation of biological hydroxyapatite. J Inorg Biochem 39:193–200
22. Penel G, Leroy G, Rey C, Sombret B, Huvenne JP, Bres E (1997) Infrared and Raman microspectrometry study of fluor- fluor-hydroxy- and hydroxy-apatites powders. J Mater Sci Mater Med 8:271–276
23. Trombe JC (1973) Decomposition et réactivité d'apatites hydroxylées et carbonatée. Ann Chim Paris 8:251–269
24. Fowler BO (1973) Infrared studies of apatites. I. Vibrational assignments for calcium, strontium and barium hydroxyapatites utilizing isotopic substitution. Inorg Chem 13:94–207
25. Tsuda H, Arends J (1994) Orientation micro-Raman spectroscopy on hydroxyapatite single crystals and human enamel crystallites. J Dent Res 73:1703–1710
26. Herzberg G (1968) Molecular spectra and molecular structure. II Infrared and Raman spectra of polyatomic molecules. D. Van Nostrand Company, London
27. Rey C, Collins B, Goehl T, Glimcher MJ (1989) The carbonate environment in bone mineral. A resolution enhanced Fourier transform infrared spectroscopy study. Calcif Tissue Int 45:157–164
28. Kaupinnen JK, Moffatt DJ, Mantsch HH, Cameron DG (1981) Fourier self-deconvolution: a method for resolving intrinsically overlapped bands. Appl Spectrosc 35:271–276
29. Pleshko N, Boskey A, Mendelsohn R (1991) Novel infrared spectroscopic method for the determination of crystallinity of hydroxyapatite minerals. Biophys J 60:786–793
30. Galadeta SJ, Paschalis EP, Betts F, Mendelsohn R, Boskey AL (1996) Fourier transform infrared spectroscopy of the solution mediated conversion of amorphous calcium phosphate to hydroxyapatite: new correlations between X-ray diffraction and infrared data. Calcif Tissue Int 58:9–16
31. Morris MD, Drumm CA (1995) Microscopic Raman line–imaging with principal component analysis. Appl Spectrosc 49:1331–1337
32. Bigi A, Boanini E, Capuccini C, Gazzano M (2007) Strontium-substituted hydroxyapatite nanocrystals. Inorg Chim Acta 360:1009–1016
33. Hadrich A, Lautié A, Mhiri T (2001) Vibrational study and fluorescence bands in the FT-Raman spectra of $Ca_{10-x}Pb_x(PO_4)_6(OH)_2$ compounds. Spectrochim Acta Part A 57:1673–1681
34. de Mul FFM, Otto C, Greve J, Arends J, ten Bosch JJ (1998) Calculation of the Raman line broadening on carbonation in synthetic hydroxyapatite. J Raman Spectrosc 19:13–21
35. He Q, Liu X, Hu X, Li S, Wang H (2011) Solid solution between lead fluorapatite and lead fluorvanadate apatite: mixing behavior, Raman feature and thermal expansivity. Phys Chem Miner 38:741–752

36. Trombe JC, Montel G (1973) Sur le spectre d'absorption infrarouge des apatites dont les tunnels contiennent des ions bivalents et des lacunes. CR Acad Sci Paris 276:1271–1274
37. Barroug A, Rey C, Trombe JC (1994) Precipitation and formation mechanism of type AB carbonate apatite analogous to dental enamel. Adv Mater Res 1–2:147–153
38. Fleet ME, Liu X (2007) Coupled substitution of type A and B carbonate in sodium bearing apatites. Biomaterials 28:916–926
39. Legeros RZ, LeGeros JP (1996) Carbonate apatite: formation and properties. Bioceramics 9:161–164
40. Quillard S, Paris M, Deniard P, Gildenhaar R, Berger G, Obadia L, Bouler JM (2011) Structural and spectroscopic characterization of a series of potassium and/or sodium-substituted β-tricalcium phosphate. Acta Biomater 7:1844–1852
41. Eichert D, Drouet C, Sfihi H, Rey C, Combes C (2007) Nanocrystalline apatite-based biomaterials: synthesis, processing and characterization. In: Kendal JB (ed) Biomaterials research advances. Nova Science, New York, pp 93–143
42. Jäger C, Welzel T, Meyer-Zaika W, Epple M (2006) A solid-state NMR investigation of the structure of nanocrystalline hydroxyapatite. Magn Reson Chem 44:573–580
43. Eichert D, Combes C, Drouet C, Rey C (2005) Formation and evolution of hydrated surface layers of apatites. Key Eng Mater 284–286:3–6
44. Brown WE, Mathew M, Chow LC (1984) Roles of octacalcium phosphate in surface chemistry of apatites. In: Misra DN (ed) Adsorption and surface chemistry of hydroxyapatite. Plenum Press, New York, pp 13–28
45. Rey C, Combes C, Drouet C, Sfihi H, Barroug A (2007) Physico-chemical properties of nanocrystalline apatites: implications for biomaterials and biominerals. Mater Sci Eng C 27:198–205
46. Leeuwenburgh SCG, Wolke JGC, de Jansen JA, Groot K (2008) Calcium phosphate coatings. In: Kokubo T (ed) Bioceramics and their clinical applications. Woodhead Publishing Limited, Cambridge, pp 464–484
47. Sun L, Berndt CC, Gross KA, Kucuk A (2001) Material fundamentals and clinical performance of plasma sprayed hydroxyapatite coatings: a review. J Biomed Mater Res 58:570–592
48. Gross KA, Berndt C, Herman H (1998) Amorphous phase formation in plasma-sprayed hydroxyapatite coatings. J Biomed Mater Res Part A 39:407–414
49. Carayon M, Lacout J-L (2003) Study of the Ca/P atomic ratio of the amorphous phase in plasma-sprayed hydroxyapatite coatings. J Solid State Chem 172:339–350
50. Demnati I, Grossin D, Combes C, Rey C (2013) Plasma sprayed apatite coatings: review of physical-chemical aspects and their biological consequences. J Med Biol Eng 34:1–7. doi:10.5405/jmbe.1459
51. Yan L, Leng Y, Weng L-T (2003) Characterization of chemical inhomogeneity in plasma-sprayed hydroxyapatite coatings. Biomaterials 24:2585–2592
52. Podlesak H, Pawlowski L, d'Haese R, Laureyns J, Lampke T, Bellayer S (2010) Advanced microstructural study of suspension plasma sprayed hydroxyapatite coatings. J Therm Spray Technol 19:657–664
53. Weinlaender M, Beumer J, Kenney EB, Moy PK (1992) Raman microprobe investigation of the calcium phosphate phases of three commercially available plasma-flame-sprayed hydroxyapatite-coated dental implants. J Mater Sci Mater Med 3:397–401
54. Demnati I, Parco M, Grossin D, Fagoaga I, Drouet C, Barykin G, Combes C, Braceras I, Goncalves S, Rey C (2012) Hydroxyapatite coating on titanium by a low energy plasma spraying mini-gun. Surf Coat Technol 206:2342–2353
55. Demnati I (2011) Développement et caractérisation de revêtements bioactifs d'apatite obtenus par projection plasma à basse énergie: application aux implants biomédicaux. PhD thesis, Institut National Polytechnique de Toulouse
56. Tadier S (2009) Etude des propriétés physico-chimiques et biologiques de ciments biomédicaux à base de carbonate de calcium: apport du procédé de co-broyage. PhD thesis, Institut National Polytechnique de Toulouse

57. Tadier S, Le Bolay N, Rey C, Combes C (2011) Co-grinding significance for calcium carbonate-calcium phosphate mixed cement. Part I: effect of particle size and mixing on solid phase reactivity. Acta Biomater 7:1817–1826
58. Cummings LJ, Snyder MA, Brisack K (2009) Protein chromatography on hydroxyapatite columns. Methods Enzymol 463:387–404
59. Tamerler C, Sarikaya M (2009) Molecular biomimetics: nanotechnology and bionanotechnology using genetically engineered peptides. Philos Trans A Math Phys Eng Sci 367:1705–1726
60. Goldberg HA, Warner KJ, Hunter GK (2001) Binding of bone sialo-protein osteopontin and synthetic polypeptides to hydroxyapatite. Connect. Tissue Res 42:25–37
61. Al-Kattan A, Errassifi F, Sautereau AM, Sarda S, Dufour P, Barroug A, Dos Santos I, Combes C, Grossin D, Rey C, Drouet C (2010) Medical potentialities of biomimetic apatites through adsorption, ionic substitution, and mineral/organic associations: three illustrative examples. Adv Eng Mater 12:B224–B233
62. Juillard A, Falgayrac G, Cortet B, Vieillard MH, Azaroual N, Hornez JC, Penel G (2010) Molecular interactions between zoledronic acid and bone: an in vitro Raman microspectroscopic study. Bone 47:895–904
63. Cukrowski I, Popovic L, Barnard W, Paul SO, van Roovyen PH, Liles DC (2007) Modeling and spectroscopic studies of bisphosphonates-bone interactions. The Raman, NMR and crystallographic investigations of Ca-HEDP complexes. Bone 41:668–678
64. Xie HN, Stevenson R, Stone N, Hernandez-Santana A, Faulds K, Graham D (2012) Tracking bisphosphonates through a 20 mm thick porcine tissue by using surface-enhanced spatially offset Raman spectroscopy. Angew Chem Int Ed Engl 51:8509–8511
65. Rodan GA, Fleisch HA (1996) Bisphosphonates: mechanisms of action. J Clin Invest 97:2692–2696
66. Pascaud P, Gras P, Coppel Y, Rey C, Sarda S (2013) Interaction between a bisphosphonate, tiludronate, and biomimetic nanocrystalline apatites. Langmuir 29:2224–2232
67. Pascaud P (2012) Apatite nanocrystallines biomimétiques comme modèles de la réactivité osseuse: étude des propriétés d'adsorption et de l'activité cellulaire d'un bisphosphonate, le tiludronate. Thesis INPT, University of Toulouse
68. Burneau A, Barres O, Gallas JP, Lavalley JC (1990) Comparative study of the surface hydroxyl groups of fumed and precipitated silicas. 2 Characterization by infrared spectroscopy of the interactions with water. Langmuir 6:1364–1372
69. Bertinetti L, Drouet C, Combes C, Rey C, Tampieri A, Coluccia S, Martra G (2009) Surface characteristics of nanocrystalline apatites: effect of Mg surface enrichment on morphology, surface hydration species, and cationic environments. Langmuir 25:5647–5654
70. Takeuchi M, Bertinetti L, Martra G, Coluccia S, Anpo M (2009) States of H_2O adsorbed on oxides: an investigation by near and mid infrared spectroscopy. Appl Catal A Gen 307:13–20
71. Ishikawa T, Wakamura M, Kondo S (1989) Surface characterization of calcium hydroxylapatite by Fourier transform infrared spectroscopy. Langmuir 5:140–144
72. Williams Q, Kettle E (1996) Infrared and Raman spectra of $Ca_5(PO_4)_6F_2$-fluorapatite at high pressures: compression-induced changes in phosphate site and Davydov splitting. J Phys Chem Solids 57:417–422
73. Xu J, Butler IS, Gilson DFR (1999) FT-Raman and high-pressure infrared spectroscopic studies of dicalcium phosphate dihydrate ($CaHPO_4{\cdot}2H_2O$) and anhydrous dicalcium phosphate (CaHPO4). Spectrochem Acta Part A 55:2801–2809
74. Xu J, Gilson DFR, Butler IS, Stangel I (1996) Effect of high external pressures on the vibrational spectra of biomedical material: calcium hydroxyapatite and calcium fluorapatite. J Biomed Mater Res 30:239–244
75. de Carmejane O, Morris MD, Davis MK, Stixrude L, Tecklenburg M, Rajachar RM, Kohn DH (2005) Bone chemical structure response to mechanical stress studied by high pressure Raman spectroscopy. Calcif Tissue Int 76:207–213
76. Fleet ME, Liu X, Liu X (2011) Orientation of channel carbonate ions in apatite: effect of pressure and composition. Am Miner 96:1148–1157

77. Carden A, Rajachar RM, Morris MD, Kohn DH (2003) Ultrastructural changes accompanying the mechanical deformation of bone tissue: a Raman imaging study. Calcif Tissue Int 72:166–175
78. Timlin JA, Carden A, Morris MD (2000) Raman spectroscopic imaging markers for fatigue-related microdamage in bovine bone. Anal Chem 72:2229–2236
79. Tsuda H, Arends J (1997) Raman spectroscopy in dental Research: a short review of recent studies. Adv Dent Res 11:539–547
80. Falgayrac G, Facq S, Leroy G, Cortet B, Penel G (2010) New method for Raman investigation of the orientation of collagen fibrils and crystallites in the Haversian system of bone. Appl Spectrosc 64:775–780
81. Rey C, Combes C, Drouet C, Glimcher MJ (2009) Bone mineral: update on chemical composition and structure. Osteoporos Int 20:1013–1021
82. Bonar LC, Roufosse AH, Sabine WK, Grynpas MD, Glimcher MJ (1983) X-ray diffraction studies of the crystallinity of bone mineral in newly synthesized and density fractionated bone. Calcif Tissue Int 35:202–209
83. Farlay D, Panczer G, Rey C, Delmas PD, Boivin G (2010) Mineral maturity and crystallinity index are distinct characteristics of bone mineral. J Bone Miner Metab 28:433–445